A novel approach to discriminate sedimentary characteristics of deltaic tidal flats with terrestrial laser scanner (TLS): Results from a case study

JIE WANG*,‡, ZHIJUN DAI*,†, SERGIO FAGHERAZZI‡ and CHUQI LONG*

*State Key Laboratory of Estuarine and Coastal Research, East China Normal University, Shanghai 200241, China

†Laboratory for Marine Geology, Qingdao National Laboratory for Marine Science and Technology, Qingdao 266237, Shandong, China

‡Department of Earth and Environment, Boston University, Boston 02215, Massachusetts, USA

Corresponding author: Prof. Zhijun Dai

State Key Laboratory of Estuarine and Coastal Research, East China Normal University, 500 Dongchuan Rd., Minhang District, Shanghai 200241, China

Email: zjdai@sklec.ecnu.edu.cn;

Tel: +86 21 62233458;

Fax: +86 21 62546441

Summary of Comments on 2022 Wang et al sed.pdf

Page: 1

Number: 1 Author: John Subject: Sticky Note Date: 10/3/2022 3:07:31 PM

Wang, J., Dai, Z., Fagherazzi, S. and Long, C., 2022. A novel approach to discriminate sedimentary characteristics of deltaic tidal flats with terrestrial laser scanner: Results from a case study. Sedimentology, 69(4), pp.1626-1648. https://doi.org/10.1111/sed.12970

ABSTRACT

Sediments in deltaic tidal flats regulate physical and chemical processes. Grain size distributions play an important role in determining sediment dynamics and substrate properties. However, it has been challenging to quantify large-scale depositional environments in intertidal flats, due to time-consuming grain size analyses and sparse sedimentary information extracted from scattered sediment samples. In this study, a novel TLS (terrestrial laser scanner)-based method was developed to characterize the substrate the of intertidal flats. We collected surface sediment samples in the Nanhui flats in the Yangtze Delta, China, and the corresponding corrected waveform amplitudes of TLS echoes at fixed sampling sites for a total of 22 months. A negative logarithmic relationship was found between the sediment sand fraction, average grain size, D_{50}, and corrected waveform amplitude of TLS echo in different hydro-meteorological conditions. The mean of average grain size of five sediment sampling sites along a transect was 58.78 μm when measured by traditional grain size analysis, and 49.48 μm when calculated with the proposed logarithmic equation, the mean with a difference of -7.99%. The mean of the absolute value of the error of average grain size at each site was up to 21.77%, which was relatively high. The mean sand and silt fraction at all sampling sites have lower errors of -9.39% and 5.01%, but the mean of all absolute errors was also as high as 27.28% and 21.75%. In addition, the two corresponding errors of the measured and TLS-based calculated D_{50} were -13.32% and 39.83%, respectively. Finally, the spatial distribution pattern of TLS-based calculated average grain size in the entire study area (Nanhui tidal flat) was figured out, it was consistent with the measured pattern with a *RMSE* of 13.83 μm. These errors could be caused by the accuracy of the TLS waveform amplitude correction and by limits of the method in recognizing different substrates. The effects produced by the presence of microphytobenthos (e.g. cyanobacterial mats or diatom biofilms) or bed forms have not been investigated and may have affected the results. TLS-based grain sizes measurements can rapidly and effectively discriminate sediment characteristics, thus avoiding traditional time-consuming measurements. We expect that the TLS-based method proposed here will have wide applications in wetland restoration and ecological protection projects, especially in inaccessible tidal flats.

Keywords:

Sediments; inversion; tidal flats; terrestrial laser scanner; grain size distribution

1. INTRODUCTION

Deltaic tidal flats develop seaward due to the accumulation of fine-grained sediments discharged by large rivers. Because of their location at the interface between land and ocean, these landforms are subject to the interaction of complex and variable terrestrial and marine processes (Short, 1991; Kane, 2008 & 2012; Coco et al., 2013; Wang et al., 2020). Land reclamation and sea level rise driven by global warming are threatening these important environments. As a result, the long-term geomorphological evolution of deltaic tidal flats has attracted the attention of many researchers in recent years (Donnelly & Bertness, 2001; Jiang et al., 2005; Fitzgerald et al., 2007; Fagherazzi et al., 2012). The substrate of tidal flats is a mixture of siliciclastic sediment (clay, silt and sand) and organic material deposited by vegetation and benthic organisms (Friedrichs, 2001; Maan et al., 2016). Sediment grain size distributions and related sedimentary structures are crucial physical-ecological indicators of intertidal flat environments; for example, intertidal biological communities vary significantly in muddy or sandy environments (Evans, 1965; Herman et al., 2001). Concentrations of alkali, metals, and nutrients also change with grain size in intertidal sediments (Zhang et al., 2002), algae survival and vegetation growths (e.g. seagrass and salt marshes) are also affected by the characteristics of the substrate (Bos et al., 2007; Park & Hwang, 2011). In addition, local sediment dynamics are closely related to grain size on muddy tidal flats (Law et al., 2013). They typically form in locations subject to enhanced siltation; the encroachment of vegetation further support accretion due to accumulation of organic matter (Swales et al., 2004; Beck et al., 2008; van Leeuwen et al., 2010). Therefore, revealing the temporal and spatial characteristics of surface sediments in tidal flats as well as, and changes in grain size distribution can help understanding sediment transport, morphological evolution, and ecological processes taking place in the substrate.

Typically, sediment characteristics can be derived from traditional grain size analyses of field samples in the laboratory. Several decades ago, sieving was used for non-cohesive sediments (Konert & Vandenberghe 1997, Munroe & McKinley, 2007), while the diameter of fine sediments was derived from Stokes sedimentation rates in a settling column. The conversion of settling velocity to particle diameter required precise measurements (Komar & Cui, 1984; Flemming, 2007). Sieving and settling columns are time-consuming methods that require a large number of sediment samples.

In recent decades, optical methods were developed to determine sediment grain sizes based on the diffraction (or scattering) of a monochromatic laser light (Swithenbank et al., 1976; Gartner et al., 2001). These methods are fast and precise, but are limited by the grain sizes of the collected sediment samples and often underestimate the fine fraction (Beuselinck et al., 1998; Murray, 2002). The laser method is a time-saving and effortless technique, which allows processing of large numbers of samples.

Recently, dynamic image analysis which is based on numerous two-dimensional projected images was introduced to measure grain sizes distributions and also determine grain shapes (Tysmans et al., 2006; Sun et al., 2019). The four methods presented above are mainly conducted in the laboratory, and have been used with success to analyze samples collected in rivers, estuaries and along coastlines.

In some settings, the collection of bottom sediments can be challenging or dangerous due to muddy substrates, inaccessibility due to tidal creeks and protected areas. This is especially true when sedimentary characteristics need to be studied across a large area. Moreover, a gradually varying topography can present subtle differences in local sedimentary environments; in these cases, methods based on few sediment samples cannot reflect the large-scale depositional variations in a tidal flat. It is therefore necessary to develop new methods that can dynamically detect large-scale sedimentary characteristics and their variations in a tidal flat. These methods can be of help in the restoration of sedimentary environments and related ecosystems.

Remote sensing provides new techniques for the analysis of surface sediments. Spectral mixture models were used on Landsat 5 imageries to map the intertidal sediment distribution in the Wash, England (Yates et al, 1993). Airborne Thematic Mapper was also applied to detect the intertidal sediment distribution in the Ribble Estuary, UK (Rainey et al., 2003). This remote sensing technique was less accurate in sandy environments than in muddy ones. The effectiveness of measuring surface grain size of riverine bedforms with airborne images at a resolution of centimeters has been assessed (Carbonneau et al., 2004). Although aerial images can provide sediment characteristics with a fine spatial scale, they are costly and only detect the distribution of the median grain size; methods detecting different sediment fractions are not available. The combination of backscattering, roughness and sediment texture, mud-content and median grain size in an intertidal surface in the Netherlands was determined from SAR imagery by van Der Wal et al. (2005). Multi-frequency radar data were also applied for the classification of tidal flat sediments (Gade et al., 2008). Although radar-based detection is not affected by weather conditions, its lower resolution is insufficient to study fine sedimentary characteristics of tidal flats. Hence, unmanned aerial systems, a multispectral camera and four multispectral sensors (covering red, green, red edge and near-infrared bands) were used to explore moisture content and median grain size in three intertidal flats, demonstrating the linkage between sediment composition and spectral characteristics (Fairley et al., 2018). The study of intertidal sediments and related geomorphic processes using remote sensing has received attention in recent years (Choi et al., 2010 & 2011; Tseng et al., 2017; Park, 2019; Kim et al., 2019). However, remote sensing inversion of sediment characteristics is often limited by spatial resolution, atmospheric disturbance, and high cost.

To determine the evolution of intertidal landforms, it is crucial to understand the spatiotemporal characteristics of intertidal sedimentary environments at the centimeter scale and their micro-geomorphic processes. To this end, it is urgent to develop a detection technology that is accurate, efficient and less labor intensive.

With the development of active and long-range remote sensing technology, laser scanners based on LiDAR (light detection and ranging) have become common. These methods include both terrestrial laser scanning (TLS) and airborne LiDAR scanning (ALS) (Tang et al., 2014; Kashani et al., 2015). TLS rapidly emits anti-interference monochromatic laser beams in succession and obtains high-precision, high-density 3D panoramic information of objects, with advantages of contactless and low risks (Bitelli et al., 2004; Hartzell et al., 2014). Here, a TLS (Riegl VZ-4000) was used to acquire intertidal point data. The instrument provides excellent long-distance measurement capability (up to 4000 m), with unique echo digitization and online waveform processing functions. Therefore, it can acquire long-distance 3D coordinates of intertidal landforms with high resolution and echo information at full waveform. The LiDAR scanner can surmount deficiencies of traditional field measurements in complex terrain providing data with high spatial resolution (Tang et al. 2015).

TLS has been widely applied to determine morphological change, vegetation biomass, and biomorphodynamic attributes in coastal and intertidal areas, due to its precision and high spatial resolution (Guarnieri et al., 2009; Owers et al., 2018). Airborne hyperspectral images and TLS data were used to analyze the mineralogical attributes of coastal dunes. Manzo et al. (2015) pointed out that grain size and mineral composition lead to essential differences in the TLS echo. Seasonal trends in the foredune ridges along the North Adriatic Sea coast (Italy) were detected using TLS-derived digital elevation models (Fabbri et al., 2017).

The combination of satellite imagery and TLS data has only recently received attention in the study of fluvial and intertidal sediments. TLS could provide analytical information on the threshold for sediment resuspension of bottom sediments (Neverman et al., 2019). Bottom echo residuals from airborne full-waveform bathymetry were isolated, and used to classify sandy and rocky seafloor sediments (Eren et al., 2018). Grain size distributions of river sandbars were accurately estimated using airborne topographic LiDAR in the Rhine River, and compared to distribution derived from photosieving results (Chardon et al., 2020).

Therefore, the TLS technology can provide grain size distribution and variations of surface sediments in tidal flats at a very high spatial and temporal resolution. Traditional studies are mostly based on a limited number of sediment samples, and therefore require interpolation to obtain spatial distributions of grain parameters (Wang & Ke, 1997; Yoo et al., 2007; Park et al., 2011; Law et al., 2013). Moreover, historical changes in sediment characteristics were often obtained from sediment cores and sedimentation profiles at low spatial resolution (Baumfalk, 1979; Ghinassi, 2007; Yamashita et al., 2009; Watson et al., 2013; Ghinassi et al., 2018a). To determine the temporal evolution of bottom sediments, multispectral images can also be used, but this method is limited by the coarse spatial resolution of the images and the low revisit period (van Der Wal et al., 2005; Fairley et al., 2018). For small-scale areas, the high accuracy and resolution of TLS is ideal for discrimination of sedimentary characteristics. Preliminary studies with this novel method have focused on sediments classification using the physical shape of the grains (Deronde et al., 2008; Engin & Maerz, 2019; Diaz-Gomez et al., 2019; Conesa-García et al., 2020). Burns and Lück-Vogel (2017) explored the relationship between sediment grain size and TLS echo intensity in the laboratory, but they did not apply the method to mixed fractions in the field.

Few studies have focused on the use of high-precision TLS to detect sediment grain size and their variations in tidal flats environments. Since the TLS echo information of different sediments is different, the utilization of TLS to reveal grain size characteristics of deltaic tidal flats is theoretically possible. Here, we use TLS to determine the sedimentary characteristics in a specific study area (140m×80m) of the Nanhui tidal flat, which is representative of the wetlands in the Yangtze Delta, China (Dai et al., 2015) (Fig. 1a-1c, Text S1). The Nanhui tidal flat is located in the southern margin of the Yangtze Delta, the open geomorphic system is dominated by strong runoff, tidal dynamics and wave power, and the surface sediments are coarse-grained. The results are compared to surface sediment samples collected in different months. The main objectives of the paper are: (i) quantify the relationship between TLS echo information and sediment grain size; (ii) improve the TLS-based method for sediment inversion in tidal flats; (iii) determine the factors affecting TLS-based results, and in particular the effect of intertidal slopes. Our results introduce a new technique for diagnosing depositional environment in large-scale tidal flats around the world.

2. DATA ACQUISITION AND METHODS

2.1 Nanhui tidal flat

The Nanhui tidal flat is located in the Nanhui Shoal which in the southern margin of the Yangtze Delta, China, the Nanhui Shoal is adjacent to the South Passage and is the fastest growing area in the delta that benefiting from previous abundant sediments transported into the subaqueous delta (Dai et al., 2015; Fan et al., 2017) (Fig. 1b). Around the Nanhui Shoal the tide forcing is semi-diurnal with an average tidal range of 2.7 m, and the mean tidal level in winter is lower than in summer (Wang et al., 2018; Wei et al., 2020). The mainly directions of ebb-flood tidal currents in the Nanhui tidal flat are parallel to local shorelines, and the dominant flood tidal current is directed southeast, the seasonal northeast waves also control the intertidal sedimentary dynamics (Fu et al., 2007; Fan et al., 2017). Over the past two decades, reclamation projects and construction of the Donghai Bridge and the seawall have modified the nearshore hydrodynamics in the Nanhui Shoal (Fig. 1b).

Specifically, the length and width of the entire study area are 140 m and 80 m, respectively, the sites of sediment sampling and TLS observations were located seaward of a reclamation seawall that near a breakwater (Fig. 1c). Sporadic patches of salt marshes (*Spartina alterniflora* and *Scirpus mariqueter*) grow on the east side with a canopy height less than 0.5 m, the intertidal elevation decreases seaward. Tidal forcing and wave power in the Nanhui tidal flat are strong, and the area experienced erosion after the construction of the artificial structures (Wang et al., 2018), as a result, sediments coarsened and are mainly sand and silty sand.

2.2 Multi-period sediment samplings

Surface sediments were regularly collected at fixed sites in the Nanhui tidal flat from January 2017 to July 2019 (Fig. 1b-1c, Table 1). The substrate was sampled in 5 cm squares with a thickness that does not exceed 0.5 cm, to minimize impact and ensure the uniformity of collected sediment properties. Each sediment sample was carefully collected using a thin hard plastic sheet and immediately stored it in a sealed and numbered plastic bag. Three different sets of sediment data were collected:

(i) Experimental sites: a total of 20 sediment sampling sites were arranged along 5 transects on June 22, 2019, and numbered from s01 to s20 (Fig. 1c, Table 1). The transects spanned different sedimentary substrates, and can therefore reveal potential couplings between sediments and corresponding waveform features of TLS echo. Fig. 1c shows transect 1 to transect 5 from west to east, all sampling sites were distributed on a bare flat with good accessibilities. Only the sediment samples s5, s6, s10 and s11 were located on the outside of the breakwater where the bottom is muddy, the other samples were collected between the seawall and the breakwater, where the bottom sediments are coarse. During the collection and observation period, some visible markers (bottles or bamboo poles) were erected behind each sampling site to mark the position and then to extract the corresponding TLS data.

(ii) Monthly sampling sites: samples were taken every month at five fixed intertidal sites (m1 to m5), during the period January 2017 to July 2019 (Fig. 1c, Table 1). The position of these five sampling sites was stable relative to the adjacent seawall, breakwaters and vegetation edges. Each monthly sampling was carried out with the same approach of the above experiment. Due to alongshore sediment transport and the sheltering effect of the breakwater, sites m4 and m5 are muddy, while the other 3 sites have a coarser grain size. Only surface sediments were collected each time. We used the monthly sediment data to explore links between grain parameters and TLS echo on a long-time scale. The two sets of data were combined in the final analysis.

(iii) Samples for validation: we utilized additional sediment data collected in 8 months (4 in winter and 4 in summer), to determine the reliability of the results. The five locations of the validation data (numbered from v1 to v5) were identical to the monthly sampling for consistency, but the sampling dates were different (Fig. 1c, Table 1). Since the tidal forcing in the Nanhui tidal flat is strong, during high tide the currents erased all substrate disturbances caused by sediment sampling.

2.3 Collection of TLS data

Both 3D coordinates and echo information of point cloud data are acquired by full-waveform TLS, including intensity angle of echoes and waveform characteristics (Hakala et al., 2012). Echo intensity is the backscattered laser signal returned by a reflected objective. The signal is recorded as a dimensionless digit; the full-waveform TLS (Riegl VZ-4000) obtains the complete waveform of one echo pulse after reflection from a specific object (Kashani et al., 2015). The echo waveform is affected by the different physical attributes of an object, and many researches have used this information to classify objects (Bitelli et al., 2004; Brodu & Lague, 2012; Koenig et al., 2015).

During the observation periods, the TLS (Riegl VZ-4000) was fixed on a tripod and placed on the seawall (the black hexagon in Fig. 1c), the working principles of TLS are illustrated in Text S2. Each observation was conducted during the lowest ebb tide, to ensure the least water accumulation in the intertidal flat and thus dry conditions. Measurements were carried out during fair weather to reduce atmospheric disturbances. The vertical and horizontal resolutions of the Riegl VZ-4000 were set approximatively to 0.004° and 0.03°, and the laser pulse frequency remained the same at 150 kHz. From January 2017 to July 2019, a total of 22 TLS datasets were collected (Table 1). The TLS observations were divided into three groups. (i) Experimental observations: point cloud data on June 22, 2019 were used to relate TLS echo waveform (amplitude and width) to sampled sediments; the same data were also used to describe the relationship between echo intensities and waveform amplitudes. (ii) Monthly observations: TLS coordinates and echo intensity of intertidal sediments were obtained in 13 monthly observations. The echo intensities were converted into waveform amplitudes based on the above experimental sites, and the relationship between waveform amplitudes and main sediment grain size parameters analyzed. (iii) Observations used for validation: we used TLS data collected in 8 months, four in winter and four in summer, to verify whether the derived relationships are reliable.

2.4 Measurements of grain size in surface sediments

Sediment samples were pre-treated as showed in Text S3. Dynamic image analysis of Camsizer XT (Retsch Technology) was used to obtain the percentage of different grain size fractions for all sediment samples. We used the moment method formulas (McManus, 1988) to calculate sediment grain size parameters (average grain size, sorting factor, skewness, and kurtosis in Text S4, Fig. 2):

$$X_{average} = \sum_{i=1}^{n} X_i * f_i / 100 \quad (1)$$

$$\delta = \sqrt{\sum_{i=1}^{n} (X_i - X_{average})^2 * f_i / 100} \quad (2)$$

$$Sk = \sqrt[3]{\sum_{i=1}^{n} (X_i - X_{average})^3 * f_i / 100} \quad (3)$$

$$Ku = \sqrt[4]{\sum_{i=1}^{n} (X_i - X_{average})^4 * f_i / 100} \quad (4)$$

where X_i is the median value of a grain size class, f_i is the percentage of this grain size class, $X_{average}$ is average grain size, δ is sorting factor, Sk and Ku are skewness and kurtosis of the distribution frequency curve of different grain size class. The percentage of different grain sizes can be obtained from the measured grain size parameters. The median grain size (D_{50}) was also calculated as the grain size corresponding to 50% of the frequency cumulative curve. Clay (0.5-4μm), silt (4-62.5μm) and sand (62.5-500 μm) fractions were quantified based on sediment classification standards developed by the American Geophysical Union. The sediments in intertidal flats were also classified according to the Shepard nomenclature (Folk & Ward, 1957). Water content was measured in the sediment samples collected on June 22, 2019 in the Nanhui tidal flat (Text S4). We first weighed each sediment sample three times with a high-precision electronic balance and took the average value as the final wet weight (W_{wet}). We then put all samples into an oven of 65°C for 48 h, and weighed them again to get dry weight (W_{dry}). Water content in 20 sediment samples (SWC) can be calculated with the following formula:

$$SWC = \left[{(W_{wet} - W_{dry})}/{W_{wet}} \right] * 100\% \tag{5}$$

2.5 Waveform decompositions and TLS amplitudes

Echo intensities (waveform amplitudes) are affected by multiple factors: distance, incidence angle, reflectivity and atmospheric attenuation (Yoon et al., 2008). Therefore, original echo information needs to be corrected before detecting the properties of different sediments. In the current normalized model of echo correction transmission distance and other parameters are averaged (Höfle & Pfeifer, 2007). In this study, the TLS echo waveform of each sediment sample was processed in the following four steps to obtain amplitude and width.

First, the location of sampled sediments was extracted from the TLS point cloud. Points within an area of 10 x 10 cm from the collected sediment sample were extracted, and their echo intensity and waveform features analyzed. Coordinates of each point cloud were converted from internal instrument coordinates to World Geodetic System (WGS1984) and the Wusong Datum (reference to theoretical lowest tidal level in the Yangtze Delta) (Fig. 1d, Fig. 2). Second, signal noise was removed from each waveform (Text S5), based on a threshold value. The threshold was determined using the standard deviation of waveform noise (σ_{noise}) after calculating the median absolute deviation, using the formulas (Persson et al., 2005):

$$\sigma_{noise} = \alpha * median\ (|f_i(t) - m|) \tag{6}$$

$$m = median(f_i(t)) \tag{7}$$

where σ_{noise} is waveform noise, α is 1.4826 (consistency factor for similar to normal distribution), $f_i(t)$ is original waveform amplitude. After calculating waveform noise, we subtract it from the original waveform. Third, the waveform was decomposed. The emitted laser pulse signal and echo signal are similar to Gaussian distributions, so that waveform data are superimposed by a series of Gaussian scattering signals. Therefore, a Gaussian model can be used to describe echo waveform of the surface sediments (Chauve et al., 2008) (Text S5).

$$y = \sum_{i=1}^{n} A_i * exp\left[-\frac{(x-\mu_i)^2}{2{\sigma_i}^2}\right] + b \quad (8)$$

where A_i is amplitude of the i Gaussian component, μ_i is the position of the peak of the i Gaussian component (distance), σ_i is standard deviation (width), n is the number of Gaussian components and b is the background noise. From the model we can obtain amplitudes, widths and distances of echo waveforms corresponding to all sediment samples. Fourth, distance and angle were corrected. Waveform amplitudes after the above decomposition are related to distance and laser incidence angle, so the amplitude needs to be corrected. The original TLS echo intensity decreases linearly with increasing distance from TLS (Fig. S1), therefore, we use this linear correction method (attenuation process) to achieve distance correction for all echo amplitudes, and reference distance (60 m) is the mean between all sediment sampling sites and TLS. The method of incident angle correction is similar to distance correction: the distance is assumed to be constant, the corrected echo amplitudes are inversely proportional to the cosine of the incident angle, the $cos\,\theta_{ref}$ is zero (Text S6, Fig. 2).

$$A_{c\_diatance} = A * ({}^{D}/_{D_{ref}}) \quad (9)$$

$$A_{c\_diatance\_angle} = A_{c\_diatance} * ({}^{cos\,\theta_{ref}}/_{cos\,\theta}) \quad (10)$$

In addition, we also calculated intertidal slope in different observation months, to analyze the seasonal relationships between slope and corresponding fitting parameters and correlations.

Substrate slope is defined in formulas 11 and 12 for the monthly observation sites m1 and m5:

$$Slope = sin^{-1}\left|{(Z_{m1} - Z_{m5})}/{D}\right| \quad (11)$$

$$D = \sqrt[2]{(X_{m1} - X_{m5})^2 + (Y_{m1} - Y_{m5})^2 + (Z_{m1} - Z_{m5})^2} \quad (12)$$

where (X_{m1}, Y_{m1}, Z_{m1}) and (X_{m5}, Y_{m5}, Z_{m5}) are the 3D coordinates of site m1 and m5, respectively (Text S7).

In this study, echo waveform features were obtained only during the experimental observations, and then used to convert corrected echo intensities observed every month to waveform amplitudes of TLS echoes. We extracted the experimental data of the two corrections to clarify the mutual relationships. The results show a very significant linear increasing trend with correlation coefficient of 0.99 (Fig. S2):

$$Intensity_c = 0.012 * Amplitude_c - 0.028 \quad (13)$$

$$Amplitude_c = 82.228 * Intensity_c + 14.390 \quad (14)$$

where $Intensity_c$ and $Amplitude_c$ is the corrected echo intensity and waveform amplitude, respectively.

After analyzing the variations in sediment grain size parameters and TLS echo amplitude characteristics of the Nanhui tidal flat, the relationships between the two data was proposed. So that we calculated the sediment average grain sizes in study area in January 2019 from the TLS echo information, to compare the consistency between the measured and TLS-based calculated results. In addition, also calculated the average grain size in June 2019 to compare their spatial patterns and seasonal variation characteristics

3. RESULTS

3.1 Grain size distributions

Grain size distributions of surface sediments in the Nanhui tidal flat measured by the Camsizer XT show the presence of spatial gradients. Along the first transect (site s01-s06), the distribution gradually changes from bimodal to unimodal moving offshore, with sand fraction declining (Fig. 3a), and average grain size decreasing from 98.28 μm to 29.46 μm (Table 2). Water fraction of the sediments increased seaward from 20.05% to 33.40% as the grain size became smaller (Table 3). Grain size variations were similar along the other transects (transects s07-s11, s12-s14, s15-s17 and s18-s20) (Fig. 3b-3d). Results indicate that overall sediments were coarser with lower water content near the seawall due to wave breaking and absence of marsh vegetation, while sediments were fine in the lower seaward tidal flat with uniform water content (between 17.89%-27.13%) (Table 2-3). Sediments were also finer along the western side, consistent with a higher elevation and the sheltering effect of the breakwater: the average grain size of transect 18-20 was only 66.54% of transect 7-8 (Table 2).

According to the Folk's triangle classification, the substrate is sand at sampling site s01 (sand fraction 91.01%), and silt at site s04, with a clay fraction of 6.3% (Fig. 3e). Six of the remaining sites were classified as silty sand and twelve as sandy silt, (Fig. 1c, Fig. 3e). Coarse sediments were located near site s07, while shoreward and near the breakwater the sediments were fine (Table 2). The silt fraction increased in summer (July 2019) with respect to winter (January 2019) (Fig. 3f).

3.2 Waveform amplitude of TLS echoes

Elevation was higher near the seawall and gradually decreased seaward, with the largest elevation difference along each transect between 0.53 m and 0.89 m (Fig. 4a). The original waveform amplitudes after the Gaussian decomposition were between 1300 and 1800, except for the lower values of 838 and 1235 at site s11 and s12, respectively. Overall and along each transect the original amplitude is not related to elevation and grain size (Fig. 4a). After distance and angle corrections, the waveform amplitudes displayed an increasing trend moving offshore, except for sites s06 and s11 (Fig. 4a). The percentage difference between the maximum and minimum amplitude for each transect was 129.79%, 175.76%, 162.74%, 60.58% and 52.10%, respectively. In addition, the elevations of the five sediment sampling sites along each transect were inversely related to the waveform amplitudes after correction (Fig. 4a). These results indicate that the lower the elevation, the finer the sediments, and the greater the corrected waveform amplitude of TLS echo (Fig. 4a).

The corrected echo intensities of monthly samples also vary in space (Fig. 4b). The maximum intensity differed from the minimum by 125.95%. The elevations of monthly sampling sites are the same as the transects, and the relationships between elevation, sediment grain size and corresponding waveform amplitude of TLS echoes is consistent with the experimental group (Fig. 4).

3.3 Relationship between corrected waveform amplitude of TLS echoes and grain size

The corrected waveform amplitudes of experimental TLS data varied between 650 and 2380, while that of monthly TLS data were mainly concentrated between 1030 and 2550 (Fig. 5). The sand fraction decreases when the amplitude increases, in accordance with a logarithmic fitting with a significant correlation ($Sand = -55.38 * ln(Amplitude_C) + 448.78$, $r = 0.68$ and $p < 0.05$) (Fig. 5a). The 65 data points of both experimental and monthly samples were regularly distributed on both sides of the log-fit curve (Fig. 5a). The silt fraction increases with amplitude, following the equation: $Silt = 54.27 * ln(Amplitude_C) - 344.44$ (r = 0.65 and $p < 0.05$) (Fig. 5b). The clay fraction was very low in all samples (51 sites had less than 5% clay), thus in the plot the points amplitude versus clay fraction are scattered and the logarithmic relationship between the two variables is not significant (Fig. 5c).

The average grain size was between 10 and 130 μm for both experimental and monthly samples; and coarser sediments had smaller standard deviation of waveform amplitudes (Fig. 6a). The amplitude and average grain sizes are linked with a negative logarithmic equation ($GS_A = -67.12 * ln(Amplitude_C) + 548.96$, r = 0.68 and $p < 0.05$), this relationship was confirmed for both experimental and monthly samples (Fig. 6a-6b). The D_{50} ranged between 130 and 170 μm, and also presents a negative logarithmic relationship with amplitude ($GS_D = -104.8 * ln(Amplitude_C) + 836.23$, r = 0.67 and $p < 0.05$) (Fig. 6c). This relationship is valid for both experimental and monthly samples (Fig. 6d).

3.4 Sediment parameters inversion based on TLS method

Based on the above logarithmic relationships, we calculated three sediment fractions, average grain size and D_{50} of each experimental and monthly sediment sample to determine the difference between laboratory measurements and TLS-based values. The clay fraction in the Nanhui tidal flat is low, so it is not considered here. Overall, TLS-based calculated values are consistent with measurements, and the corresponding Root Mean Square Errors (RMSE) of sand fraction, silt fraction, average grain size and D_{50} are 20.09%, 19.28%, 22.68 μm and 34.56 μm, respectively (Fig. 7a-7b); the Mean Absolute Deviation (MAD) are 16.24%, 15.87%, 17.89 μm and 28.97μm. Mean values and standard deviations were also calculated for each monthly sample (Fig. 7e-7h). The mean sand fraction derived from the log regression is 36.66% for the five monthly samples, which underestimates by 9.39% the values measured in the lab (40.46%, Table 4). The sampling site closest to the TLS station has the greatest relative deviation between the two values (Table 4; Fig. 7e). The mean silt fraction is overestimated by 5.01% (Table 4). The standard deviation of the measured values at the seaward sampling sites is higher than the TLS-based values (Fig. 7f). Furthermore, the calculated mean values of average grain size and D_{50} are 7.99% and 13.32% lower than the measured ones (Table 4), the relative deviations of the middle sites are small (Fig. 7g-7h). In general, except for the clay fraction that is low and variable, the new method of estimating surface sediment characteristics from TLS waveform amplitudes is reliable. The mean of measured and TLS-based calculated average grain size of five sediment sampling sites along a transect was 58.78 μm and 49.48 μm, respectively, shows a difference of -7.99%. In addition, the mean of the absolute value of the error of average grain size at each site was up to 21.77%, which was relatively high. Moreover, the mean sand and silt fraction at all sampling sites have lower errors of -9.39% and 5.01%, but the mean of all absolute errors was also as high as 27.28% and 21.75%.

4. DISCUSSION

4.1 Physical meaning of the coefficients in the inversion equations

The sand fraction in the Nanhui tidal flat gradually decreases seaward, while the silt fraction increases. The clay fraction is only around 5%. The grain size increases shoreward and to the East. Areas with low elevation are characterized by fine-grained sediments carried by tidal currents, due to retention effect of the breakwater. These different sedimentary environments are an excellent test for determining the relationships between sediment parameters and TLS waveform amplitudes (Collin et al., 2010; Medjkane et al., 2018). Sand/silt fractions and average/median grain size showed a significant logarithmic correlation with TLS waveform amplitudes. We also found a significant logarithmic relationship between the corrected waveform amplitudes and waveform widths. This relationship can be used for future sediment classifications (Fig. S3).

The determined relationships give us the opportunity to explore sedimentological variations in different seasons. To do that, we separately analyzed the logarithmic fitting equations ($y=a*ln(x)+b$) and their coefficients for 15 monthly sampling data (Table S1). In general, the larger the correlation coefficient, the higher is the absolute value of the parameter a, which means that the logarithm curve declines faster, so that the variations in sediment average grain size is greater in winter (Fig. 8a). At the same time, the parameter b increases with an increase in the correlation coefficient, indicating that coarser grain size distributions yield a better fitting (Fig. 8b). The larger the bottom slope, the smaller is the correlation coefficient, indicating that slope steepening due to erosion in summer produces coarser sediment grain size along the transect (Fig. 8c). The relationship between parameters a and b and intertidal slope reflect above variation differences of coefficients a and b (Fig. 8d-8e). In winter, weaker wave forcing and lower mean tidal levels relative to summer reduce the deposition of fine sediments, leading to smaller variations in grain size along transect m1-m5. Therefore, the parameters a and b in the logarithmic fitting equation are related to seasonal hydrodynamic conditions that control the spatial regularity of the sediment characteristics. Despite seasonal variations, sediment parameters and corrected TLS waveform amplitudes maintain significant logarithmic relationships (Fig. 5-6).

4.2 Validation and possible sources of uncertainty

A subset of monthly sediment samples was used to validate the logarithmic relationships for sand and silt fractions, average grain size and D_{50}. The relationships derived from the validation data compare well to the relationships derived from the experimental and monthly data (Fig. 9a-9d), indicating the effectiveness and robustness of the TLS-based method. Moreover, we compare the sediment parameters derived from the logarithmic equations of the validation data with the values measured in the laboratory (Fig. 9e-9h). The RMSEs of sand fraction, silt fraction, average grain size, and D_{50} are 17.17%, 16.68%, 24.86 μm and 33.06 μm (Fig. 9e-9h), which differ from the values of experimental and monthly collected sediments by -14.57%, -12.85%, 9.60% and -4.33%, respectively. The difference in MAEs is even lower: -7.43%, -9.40%, 13.94% and 0.86% respectively (Fig. 9e-9h); the study results and the validation results are therefore consistent.

Previous studies have shown that sandy sediments in the Yangtze Delta have a terrestrial origin with terrigenous detrital minerals (mainly quartz and feldspar); the substrate material of the Nanhui tidal flat is consistent with those data (Cao et al., 2018). Sandy substrates of tidal flats are relatively loose with high porosity, and are eroded by waves during flooding (especially in summer). On the other hand, silty/clay sediments are mainly composed of clay minerals (illite, kaolinite and chlorite etc.), which is widely distributed in the Nanhui tidal flat and the Yangtze Delta. Because fine-grained minerals adhere together, the porosity is smaller, and the backscattering of the near-infrared laser stronger (Burton et al., 2011). Sediments distribution in this tidal flat is dominated by intertidal hydrodynamics and disturbances from the breakwater or marsh vegetation (Fig 1c and Fig. 3a-3d). Differences in echo intensity were also used in other studies of sediments identification and classification (Brennan & Webster, 2006; Tulldahl & Wikström, 2012; Fabbri et al., 2017).

Microphytobenthos (e.g. cyanobacterial mats or diatom biofilms) can also alter the properties of sediments with their extracellular polymeric substance (EPS) that adheres to sediment surfaces (De Jorge et al., 1995; Méléder et al., 2005; Andersen et al., 2010). EPS thickness is comparable to the diameter of fine sand (Herlory et al., 2004; Stal, 2010), thus affecting the TLS echo intensity. The effect of microphytobenthos requires further detailed investigations. In our study area, the wave action is strong, favoring coarse bottom sediments with low water content (Zhu et al., 2014; Wei et al., 2020). The tidal flat in study area has been eroded by about 80-100 cm since 2016, and the erosional regime has prevented the formation of microphytobenthos in recent years (Fig. S4-S5; Wang et al., 2018). Therefore, the sediments at study sites are coarse-grained sand or sandy silty sand with a tendency to further coarsening (Fig. 3; Wei et al., 2020). van de Koppel et al. (2001) studied the positive feedback between the development processes of benthic diatoms and the erosion of silty sediments in the Molenplaat tidal flat of Westerschelde Estuary, Netherlands, pointed out when the geomorphic change were dominated by erosion under middle-high bed shear stress, the diatom cover were low. Garwood et al. (2015) also indicated mud biofilms will be mainly preserved in fine sediments (clays or very fine silts) in sediments that collected from the intertidal flat of the Fundy Bay, Canada. Moreover, Mariotti and Fagherazzi (2012) proposed a novel biofilm growth model in shallow coastal areas and found that the biofilm mass was affected by strong tidal forcing and wave power, thus the strong hydrodynamics will greatly restrict its growth.

Indeed, the existences of microphytobenthos contribute to the biostabilization of tidal flats by increasing the erosion threshold (Wooldridge et al., 2017; Kim et al., 2021). However, the growth and total mass of microphytobenthos in tidal flats with continuous strong erosion are challenged. In fact, the tidal forcing and wave power in the Nanhui tidal flat are strong, there was no obvious large-scale presence of microphytobenthos during all observation periods in the study area. Therefore, although the effect of the presence of microphytobenthos on the efficacy of this TLS-based method was not verified in the current study, we speculate that its impacts on TLS echo intensity is relatively limited in this studied. But we must carefully recognize that, the specificities of current study area (strong hydrodynamics, coarse-grained sediments, erosive geomorphic processes) and relevant results, in other situations, where biota and bedforms are present and the material is muddier, this TLS-based method maybe not work very well. In the future, more detailed experiments and understanding are required to quantify the different influencing factors, so that it can be applied to other types of tidal flats.

Intertidal microtopography (e.g. sand ripples) may also affect TLS measurements. Both microphytobenthos and bedforms could in theory selectively change the TLS echo intensity as a function of grain size. Ripples are only present in non-cohesive sediments, increasing the roughness of the substrate. Microphytobenthos are more common in cohesive bottom sets, giving rise to biofilm patches. This notwithstanding, the relationships between TLS echo intensity and grain size parameters are significant at our study site, indicating that we can still derive important information about bottom grain size, and treat microphytobenthos and bedforms as possible sources of error. More experiments are clearly needed to address the effect of these processes on grain size distribution and reduce the uncertainty of the measurements.

Other challenges in detecting surface sediments in tidal flats need to be recognized, such as the influence of vegetation and ponds. A dense vegetation canopy can obstruct the laser beam, thereby reducing the number of echoes bouncing from the substrate (Schmid et al., 2011; Ward et al., 2013; Rayner et al., 2021). The laser signal cannot penetrate ponding water. In these cases, manual samplings are still required to compensate for the absence of TLS data. It is also crucial to establish separate relationships for sediment grain parameters in bare flats and sheltered areas, where vegetation and biofilms are more common.

4.3 Factors controlling waveform amplitude of TLS echo

Robust corrections of waveform amplitudes or echo intensities are critical for the proposed TLS method. Multiple potential influencing factors must be considered, which mainly relate to operation stability of the TLS instrumental sensors, atmospheric conditions (transparency, humidity, etc.), and backscattering characteristics of surface sediments (Hopkinson et al., 2004; Yoon et al., 2008; Hancock et al., 2015). Here, the experimental, monthly and validation TLS observations were all carried out in fair weather, with clear sky and low tidal levels. Hence, the intensity attenuation during atmospheric transmission can be ignored. We only corrected for waveform amplitudes and differences in echo intensities caused by distance and beam angle, and analyzed laser scattering characteristics that are directly associated to the physical organization of intertidal sediments.

Because the TLS (Riegl VZ-4000) operates in the near-infrared band, water content will absorb part of the laser energy (Ehret et al., 1993; Hartzell et al., 2014). Both Unmanned Aerial Vehicle images and original TLS point cloud data showed that there are some wet areas in the Nanhui intertidal flat (Fig. 1c-1d). And the actual measurements indicate that water content in the samples was about 17.89%-34.51%. Therefore, in this study we chose sampling sites without water accumulation, and also tried to maintain the same position of the TLS tripod on the seawall for all 22 measurements. Further research is needed to explore the attenuation effect of water absorption in the echo waveform amplitude (Nield et al., 2014). In addition, TLS observation is also restricted by tidal hydrodynamic conditions. As tidal flats are generally affected by wetting and drying, the substrate is only exposed during low tide with the least water accumulation (Choi et al., 2010; Fairley et al., 2018). As a result, the time suitable for observation is relatively short. In the future, it will be necessary to explore the practicality of airborne LiDAR due to its large-scale and long-distance detection capabilities (Lang et al., 2009; Richard et al., 2013; Chardon et al., 2020).

4.4 Application of the new TLS method to study intertidal dynamics

With an interpolation of all experimental sediment samples we obtained the spatial distribution of average grain size in the Nanhui tidal flat in June 2019 (Fig. 10a). A similar distribution was obtained from the TLS data using the logarithmic equations here (Fig. 10b). Both distributions indicate that sediments become gradually finer seaward with the presence of longitudinal subzones. Average grain size patterns are similar in the collected sediments and in the TLS-based inversion map, with a corresponding mean grain size of 66.43 µm and 65.07 µm, respectively (error of 2.05%) (Fig. 10a-10b). The measured and TLS-based average grain size have a significant correlation ($r = 0.88$, $p < 0.01$) with a Root Mean Square Error of 13.83 µm. The comparison shows that TLS method tends to overestimate the average grain size of sediments in the high value interval (Fig. 10c). Since the measured distribution is derived through interpolation of 20 sampling points in a grid, the maximum deviation between measured and calculated values is at both ends of the transects (Fig. 10c). The sediment map was also derived from TLS data collected in January 2019 (Fig. 10d). The average grain size was 71.46 μm, which means that sediments are coarser in winter. Frequency distributions also indicate that the sand fraction increases and the silt fraction decreases in winter (Fig. 10e).

Although the measured and calculated experimental-monthly sediment grain size parameters were relatively scattered (Fig. 5, 6 and 7a-7d), when revealing the spatial distribution pattern of the sediment average grain size in the study area, this TLS-based method shows acceptable reliability (Fig 10a-10c). Indeed, the experimental-monthly sediment sampling sites are limited and spatially dispersed, and some potential factors will affect the correction effectiveness of the TLS echo amplitude/intensity in our results, which is likely responsible for those scattered data points, also need further studies. In the Nanhui tidal flat, the distribution of sediment grain size parameters and their TLS echo intensities are relatively continuous and smooth. The TLS-based calculated average grain size can alleviate the deficiency that the correlation mentioned above needs to be improved to some extent, so as to reveal the spatial distribution characteristics in the Nanhui tidal flat, but it is necessary to further improve the accuracy.

The TLS approach provides new opportunities for the determination of sediment characteristics in tidal environment, but there are still some technical limitations (correction algorithms, presence of biota) that need to be improved, especially in specific micro-topographic areas. The new method does not require repetitive sediment samplings in the field and time-consuming analyses in the laboratory (Flemming, 2007; Ahn, 2012; Park, 2019). Furthermore, traditional methods cannot determine variations in sediment characteristics at high spatial resolution because of the limited number of sampling sites.

More detailed laboratory experiments are needed to clarify the effects of different mineral components on laser backscatter characteristics. The parameters of the logarithmic fitting curves are related to the seasonal sedimentary dynamics and morphodynamic processes. Moreover, our proposed method can be used to explore relationships between sediment grain size and other geophysical and environmental processes, such as wave shear stresses, elevation, nutrients and soil carbon pools (Rosser et al., 2005; van Leeuwen et al., 2011; Ghinassi et al., 2018b; Brand et al., 2019; Wiggins et al., 2019).

5. CONCLUSIONS

The sediment characteristics of deltaic tidal flats are affected by complex terrestrial and oceanic hydrodynamics. In this study, a high-precision full-waveform TLS was used to reveal sediment parameters in the Nanhui tidal flat, Yangtze Delta, China. We collected surface sediment samples from the Nanhui tidal flat and compared their grain size distributions to corresponding corrected waveform amplitudes of TLS echo in different hydrometeorological scenarios, for a total of 22 months. The main results and conclusions are as follows:

(1) The sediment sand fraction, average grain size and D_{50} decrease seaward, while the corrected waveform amplitude of TLS echo increases. This spatial variation is consistent with a decrease in elevation in the Nanhui tidal flat. (2) Based on the data, logarithmic equations were constructed to retrieve sediment grain size (fractions, average and D_{50}) from detected TLS waveform amplitudes. The mean of measured and TLS-based calculated sediment average grain size of five monthly sites along the sampling transect was 58.78 μm and 49.48 μm, respectively,

besides, the mean D_{50} was 67.32 μm and 58.35 μm. Overall, the errors of mean values of sediment grain size parameters along the transect were small, but the mean of the absolute value of the error at each sampling site were relatively high. (3) The parameters of the proposed logarithmic equations are affected by the spatial regularity of the grain size distributions. In winter, the weaker hydrodynamic conditions and the gentle geomorphic slopes result in higher fitting correlations.

We must carefully recognize the specificity of current study area, the Nanhui tidal flat, with strong hydrodynamics and coarse-grained sediments. This TLS-based method maybe not work very well in some tidal flat or wetland, where microphytobenthos (e.g. cyanobacterial mats or diatom biofilms) are present and the substrate is muddier or area sheltered by salt marsh vegetation. In future studies, more specific experiments will be conducted to understand the relationship between TLS waveform amplitude and the sediment physical characteristics, to quantify the different influencing factors, so that it can be applied to other types of tidal tidal flats. Grain size distributions obtained from the new TLS method can be used as indicators of sedimentary dynamics, shedding light on environmental processes affecting biological habitats.

ACKNOWLEDGMENTS

This research presented was supported by Key Projects of Intergovernmental Science and Technology Innovation Cooperation of the Ministry of Science and Technology in China (No. 2018YFE0109900), the International Science and Technology Cooperation Foundation Projects of Shanghai Science and Technology Commission (No. 19230712400), the ECNU Academic Innovation Promotion Program for Excellent Doctoral Students (No. YBNLTS2019-008) of

Fundamental Research Funds for the Central Universities. Sergio Fagherazzi was partly funded by the USA National Science Foundation award 1637630 (PIE LTER) and 1832221 (VCR LTER). We are really grateful to Dr. Ian Kane, Dr. Massimiliano Ghinassi and three anonymous reviewers for their time and constructive comments and suggestions that significantly helped to improve this manuscript.

DATA AVAILABILITY STATEMENT

The data that support the findings of this study are available from the corresponding author (Prof. Zhijun Dai) upon reasonable requests. Other data elucidating the findings of this study are provided in supplementary information files.

SUPPLEMENTARY INFORMATION

The Supplementary Information is available free of charge, which consists of Texts S1-S7, Figures S1-S5 and Tables S1.

REFERENCES

Ahn, J.H. (2012) Size distribution and settling velocities of suspended particles in a tidal embayment. Water Res., 46(10), 3219-3228.

Andersen, T.J., Lanuru, M., Van Bernem, C., Pejrup, M. and Riethmueller, R. (2010) Erodibility of a mixed mudflat dominated by microphytobenthos and Cerastoderma edule, East Frisian Wadden Sea, Germany. Estuar. Coast. Shelf Sci., 87(2), 197-206.

Baumfalk, Y.A. (1979) Heterogeneous grain size distribution in tidal flat sediment caused by bioturbation activity of Arenicola marina (Polychaeta). Netherlands J. Sea Res., 13(3-4), 428-440.

Beck, M., Dellwig, O., Liebezeit, G., Schnetger, B. and Brumsack, H.J. (2008) Spatial and seasonal variations of sulphate, dissolved organic carbon, and nutrients in deep pore waters of intertidal flat sediments. Estuar. Coast. Shelf Sci., 79(2), 307-316.

Beuselinck, L., Govers, G., Poesen, J., Degraer, G. and Froyen, L. (1998) Grain-size analysis by laser diffractometry: comparison with the sieve-pipette method. Catena, 32(3-4), 193-208.

Bitelli, G., Dubbini, M. and Zanutta, A. (2004) Terrestrial laser scanning and digital photogrammetry techniques to monitor landslide bodies. Int. Arch. Photogramm., Remote Sens. and Spat. Inf. Sci., 35(B5), 246-251.

Bos, A.R., Bouma, T.J., de Kort, G.L. and van Katwijk, M.M. (2007) Ecosystem engineering by annual intertidal seagrass beds: sediment accretion and modification. Estuar. Coast. Shelf Sci., 74(1-2), 344-348.

Brand, E., De Sloover, L., De Wulf, A., Montreuil, A.L., Vos, S. and Chen, M. (2019) Cross-shore suspended sediment transport in relation to topographic changes in the intertidal zone of a macro-tidal beach (Mariakerke, Belgium). J. Mar. Sci. Eng., 7(6), 172.

Brennan, R. and Webster, T.L. (2006) Object-oriented land cover classification of lidar-derived surfaces. Can. J. Remote Sens., 32(2), 162-172.

Brodu, N. and Lague, D. (2012) 3D terrestrial lidar data classification of complex natural scenes using a multi-scale dimensionality criterion: Applications in geomorphology. ISPRS-J. Photogramm. Remote Sens., 68, 121-134.

Burns, J. and Lück-Vogel, M. (2017) Using LiDAR derivatives to estimate sediment grain size on beaches in False Bay. International Symposium for Remote Sensing of the Environment, Tshwane, South Africa, May 8-12, 2017.

Burton, D., Dunlap, D.B., Wood, L.J. and Flaig, P.P. (2011) Lidar intensity as a remote sensor of rock properties. J. Sediment. Res., 81(5), 339-347.

Cao, C., Cai, F., Zheng, Y.L., Wu, C.Q., Lu, H.Q., Bao, J.J. and Sun, Q. (2018) Temporal and spatial characteristics of sediment sources on the southern Yangtze Shoal over the Holocene. Sci. Rep., 8(1), 1-12.

Carbonneau, P.E., Lane, S.N. and Bergeron, N.E. (2004) Catchment-scale mapping of surface grain size in gravel bed rivers using airborne digital imagery. Water Resour. Res., 40(7), 1-11.

Chardon, V., Schmitt, L., Piégay, H. and Lague, D. (2020) Use of terrestrial photosieving and airborne topographic LiDAR to assess bed grain size in large rivers: a study on the Rhine River. Earth Surf. Process. Landf., 45(10), 2314-2330.

Chauve, A., Mallet, C., Bretar, F., Durrieu, S., Deseilligny, M.P. and Puech, W. (2008) Processing full-waveform lidar data: modelling raw signals. In International archives of photogrammetry, remote sensing and spatial information sciences 2007, 102-107.

Choi, J.K., Ryu, J.H., Lee, Y.K., Yoo, H.R., Woo, H.J. and Kim, C.H. (2010) Quantitative estimation of intertidal sediment characteristics using remote sensing and GIS. Estuar. Coast. Shelf Sci., 88(1), 125-134.

Choi, J.K., Eom, J. and Ryu, J.H. (2011) Spatial relationships between surface sedimentary facies distribution and topography using remotely sensed data: Example from the Ganghwa tidal flat, Korea. Mar. Geol., 280(1-4), 205-211.

Coco, G., Zhou, Z., Van Maanen, B., Olabarrieta, M., Tinoco, R. and Townend, I. (2013) Morphodynamics of tidal networks: advances and challenges. Mar. Geol., 346, 1-16.

Collin, A., Long, B. and Archambault, P. (2010) Salt-marsh characterization, zonation assessment and mapping through a dual-wavelength LiDAR. Remote Sens. Environ., 114(3), 520-530.

Conesa-García, C., Puig-Mengual, C., Riquelme, A., Tomás, R., Martínez-Capel, F., García-Lorenzo, R., Pastor, J,L., Pérez-Cutillas, P. and Cano Gonzalez, M. (2020) Combining SfM photogrammetry and terrestrial laser scanning to assess event-scale sediment budgets along a gravel-bed ephemeral stream. Remote Sens., 12(21), 3624.

Dai, Z.J, Liu, J.T. and Wen, W. (2015) Morphological evolution of the south passage in the Changjiang (Yangtze River) estuary, China. Quat. Int., 380, 314-326.

Diaz-Gomez, R., Pasternack, G.B., Guillon, H., Byrne, C.F. and Sandoval Solis, S. (2019) Can airborne lidar point clouds quantify grain size contributions to ground sediment facies? AGU Fall Meeting Abstracts, EP11C-2137.

De Jorge, V.N. and van Beusekom, J.E.E. (1995) Wind- and tide-induced resuspension of sediment and microphytobenthos from tidal flats in the Ems estuary. Limnol. Oceanogr., 40(4), 776-778.

Deronde, B., Houthuys, R., Henriet, J.P. and Lancker, V.V. (2008) Monitoring of the sediment dynamics along a sandy shoreline by means of airborne hyperspectral remote sensing and LIDAR: a case study in Belgium. Earth Surf. Processes Landforms, 33(2), 280-294.

Donnelly, J.P. and Bertness, M.D. (2001) Rapid shoreward encroachment of salt marsh cordgrass in response to accelerated sea-level rise. Annu. Rev. Earth Planet. Sci., 98(25), 14218-14223.

Ehret, G., Kiemle, C., Renger, W. and Simmet, G. (1993) Airborne remote sensing of tropospheric water vapor with a near–infrared differential absorption lidar system. Appl. optics, 32(24), 4534-4551.

Engin, I.C. and Maerz, N.H. (2019) Size distribution analysis of aggregates using LiDAR scan data and an alternate algorithm. Measurement, 143, 136-143.

Eren, F., Pe'eri, S., Rzhanov, Y. and Ward, L. (2018) Bottom characterization by using airborne lidar bathymetry (ALB) waveform features obtained from bottom return residual analysis. Remote Sens. Environ., 206, 260-274.

Evans, G. (1965) Intertidal flat sediments and their environments of deposition in the Wash. Q. J. Geol. Soc. London, 121(1-4), 209-240.

Fabbri, S., Giambastiani, B.M., Sistilli, F., Scarelli, F. and Gabbianelli, G. (2017) Geomorphological analysis and classification of foredune ridges based on Terrestrial Laser Scanning (TLS) technology. Geomorphology, 295, 436-451.

Fagherazzi, S., Kirwan, M.L., Mudd, S.M., Guntenspergen, G.R., Temmerman, S., D'Alpaos, A., Van De Koppel, J., Rybczyk, J.M., Reyes, E., Craft, C. and Clough, J. (2012) Numerical models of salt marsh evolution: Ecological, geomorphic, and climatic factors. Rev. Geophys., 50(1), 1-28.

Fu, G., Li, J., Ying, M. and Yu, Z. (2007) Analysis on Recent Topography evolution of Nanhuizui tidal flat in Yangtze Estuary. Mar. Sci. Bull., 26(2), 105-112.

Fan, D.D., Wu, Y.J., Zhang, Y., Burr, G., Huo, M. and Li, J. (2017) South Flank of the

Yangtze Delta: Past, present, and future. Mar. Geol., 392, 78-93.

Fairley, I., Mendzil, A., Togneri, M. and Reeve, D.E. (2018) The Use of Unmanned Aerial Systems to Map Intertidal Sediment. Remote Sens., 10(12), 1918.

Flemming, B.W. (2007) The influence of grain-size analysis methods and sediment mixing on curve shapes and textural parameters: implications for sediment trend analysis. Sediment. Geol., 202(3), 425-435.

Folk, R.L. and Ward, W.C. (1957) A study in the significance of grain size parameters. J. Sediment. Res., 27(1), 3-26.

FitzGerald, D.M., Fenster, M.S., Argow, B.A. and Buynevich, I.V. (2008) Coastal impacts due to sea-level rise. Annu. Rev. Earth Planet. Sci., 36(1), 601-647.

Friedrichs, C.T. and Perry, J.E. (2001) Tidal salt marsh morphodynamics: a synthesis. J. Coast. Res., 7-37.

Gade, M., Alpers, W., Melsheimer, C. and Tanck, G. (2008) Classification of sediments on exposed tidal flats in the German Bight using multi-frequency radar data. Remote Sens. Environ., 112(4), 1603-1613.

Gartner, J.W., Cheng, R.T., Wang, P.F. and Richter, K. (2001) Laboratory and field evaluations of the LISST-100 instrument for suspended particle size determinations. Mar. Geol., 175(1-4), 199-219.

Garwood, J.C., Hill, P.S., MacIntyre, H.L. and Law, B. A. (2015). Grain sizes retained by diatom biofilms during erosion on tidal flats linked to bed sediment texture. Cont. Shelf Res., 104, 37-44.

Ghinassi, M. (2007) The effects of differential subsidence and coastal topography on highorder transgressive-regressive cycles: Pliocene nearshore deposits of the Val d'Orcia Basin, Northern Apennines, Italy. Sediment. Geol., 202(4), 677-701.

Ghinassi, M., Brivio, L., D'Alpaos, A., Finotello, A., Carniello, L., Marani, M. and Cantelli, A. (2018a) Morphodynamic evolution and sedimentology of a microtidal meander bend of the Venice Lagoon (Italy). Mar. Pet. Geol., 96, 391-404.

Ghinassi, M., D'alpaos, A., Gasparotto, A., Carniello, L., Brivio, L., Finotello, A., Roner, M., Franceschinis, E., Realdon, N., Howes, N. and Cantelli, A. (2018b). Morphodynamic evolution and stratal architecture of translating tidal point bars: Inferences from the northern Venice Lagoon (Italy). Sedimentology, 65(4), 1354-1377.

Guarnieri, A., Vettore, A., Pirotti, F., Menenti, M. and Marani, M. (2009) Retrieval of small-relief marsh morphology from Terrestrial Laser Scanner, optimal spatial filtering, and laser return intensity. Geomorphology, 113(1-2), 12-20.

Hancock, S., Armston, J., Li, Z., Gaulton, R., Lewis, P., Disney, M., Danson, F.M., Strahler, A., Schaaf, C., Anderson, K. and Gaston, K.J. (2015) Waveform lidar over vegetation: An evaluation of inversion methods for estimating return energy. Remote Sens. Environ. 164, 208-224.

Hakala, T., Suomalainen, J., Kaasalainen, S. and Chen, Y.W. (2012) Full waveform hyperspectral LiDAR for terrestrial laser scanning. Opt. Express, 20(7), 7119-7127.

Hartzell, P., Glennie, C., Biber, K. and Khan, S. (2014) Application of multispectral LiDAR to automated virtual outcrop geology. ISPRS-J. Photogramm. Remote Sens., 88, 147-155.

Herlory, O., Guarini, J.M., Richard, P. and Blanchard, G.F. (2004) Microstructure of microphytobenthic biofilm and its spatio-temporal dynamics in an intertidal mudflat

(Aiguillon Bay, France). Mar. Ecol. Prog. Ser., 282, 33-44.

Herman, P.M., Middelburg, J.J. and Heip, C.H. (2001) Benthic community structure and sediment processes on an intertidal flat: results from the ECOFLAT project. Cont. Shelf Res., 21(18-19), 2055-2071.

Höfle, B. and Pfeifer, N. (2007) Correction of laser scanning intensity data: Data and model-driven approaches. ISPRS-J. Photogramm. Remote Sens., 62(6), 415-433.

Hopkinson, C., Chasmer, L., Young-Pow, C. and Treitz, P. (2004) Assessing forest metrics with a ground-based scanning lidar. Can. J. For. Res., 34(3), 573-583.

Jiang, W., Li, J., Wang, W., Xie, Z. and Mai, S. (2005) Assessment of wetland ecosystem health based on RS and GIS in Liaohe River Delta. In Proceedings. 2005 IEEE International Geoscience and Remote Sensing Symposium, 2384-2386.

Kane, I.A., McCaffrey, W.D. and Peakall, J. (2008) Controls on sinuosity evolution within submarine channels. Geology, 36(4), 287-290.

Kane, I.A. and Pontén, A.S. (2012) Submarine transitional flow deposits in the Paleogene Gulf of Mexico. Geology, 40(12), 1119-1122.

Kashani, A.G., Olsen, M.J., Parrish, C.E. and Wilson, N. (2015) A review of LiDAR radiometric processing: From ad hoc intensity correction to rigorous radiometric calibration. Sensors, 15(11), 28099-28128.

Kim, B., Lee, J., Noh, J., Bae, H., Lee, C., Ha, H.J., Hwang, K, Kim, D.U., Kwonc, B.O., Ha, H.K., Pierred, G., Delattred, C., Michaud, P. and Khim, J.S. (2021). Spatiotemporal variation of extracellular polymeric substances (EPS) associated with the microphytobenthos of tidal flats in the Yellow Sea. Mar. Pollut. Bull., 171, 112780.

Kim, K.L., Kim, B.J., Lee, YK. and Ryu, J.H. (2019) Generation of a large-scale surface sediment classification map using unmanned aerial vehicle (UAV) data: A case study at the Hwang-do tidal flat, Korea. Remote Sensing, 11(3), 229.

Komar, P.D. and Cui, B. (1984) The analysis of grain-size measurements by sieving and settling-tube techniques. J. Sediment. Res., 54(2), 603-614.

Konert, M. and Vandenberghe, J.E.F. (1997) Comparison of laser grain size analysis with pipette and sieve analysis: a solution for the underestimation of the clay fraction. Sedimentology, 44(3), 523-535.

Koenig, K., Höfle, B., Hämmerle, M., Jarmer, T., Siegmann, B. and Lilienthal, H. (2015) Comparative classification analysis of post-harvest growth detection from terrestrial LiDAR point clouds in precision agriculture. ISPRS-J. Photogramm. Remote Sens., 104, 112-125.

Lang, M.W. and McCarty, G.W. (2009) Lidar intensity for improved detection of inundation below the forest canopy. Wetlands, 29(4), 1166-1178.

Law, B.A., Milligan, T.G., Hill, P.S., Newgard, J., Wheatcroft, R.A. and Wiberg, P.L. (2013) Flocculation on a muddy intertidal flat in Willapa Bay, Washington, Part I: A regional survey of the grain size of surficial sediments. Cont. Shelf Res., 60, 136-S144.

Maan, D.C., van Prooijen, B.C., Wang, Z.B. and De Vriend, H.J. (2015) Do intertidal flats ever reach equilibrium? J. Geophys. Res.-Earth Surf., 120(11), 2406-2436.

Manzo, C., Valentini, E., Taramelli, A., Filipponi, F. and Disperati, L. (2015) Spectral characterization of coastal sediments using field spectral libraries, airborne hyperspectral images and topographic LiDAR data (FHyL). Int. J. Appl. Earth Obs. Geoinf., 36, 54-68.

Mariotti, G. and Fagherazzi, S. (2012). Modeling the effect of tides and waves on benthic biofilms. J. Geophys. Res.: Biogeosci., 117(G4).

McManus, J. Grain size determination and interpretation. In: Tucker, M. (Ed.) Techniques in Sedimentology, Blackwell, Oxford, 63-85.

Medjkane, M., Maquaire, O., Costa, S., Roulland, T., Letortu, P., Fauchard, C. and Davidson, R. (2018) High-resolution monitoring of complex coastal morphology changes: cross-efficiency of SfM and TLS-based survey (Vaches-Noires cliffs, Normandy, France). Landslides, 15(6), 1097-1108.

Méléder, V., Barillé, L., Rincé, Y., Morançais, M., Rosa, P. and Gaudin, P. (2005) Spatio-temporal changes in microphytobenthos structure analysed by pigment composition in a macrotidal flat (Bourgneuf Bay, France). Mar. Ecol. Prog. Ser., 297, 83-99.

Munroe, D. and McKinley, R.S. (2007) Commercial Manila clam (Tapes philippinarum) culture in British Columbia, Canada: the effects of predator netting on intertidal sediment characteristics. Estuar. Coast. Shelf Sci., 72(1-2), 319-328.

Murray, M.R. (2002) Is laser particle size determination possible for carbonate-rich lake sediments? J. Paleolimn., 27(2), 173-183.

Neverman, A.J., Fuller, I.C., Procter, J.N. and Death, R.G. (2019) Terrestrial laser scanning and structure-from-motion photogrammetry concordance analysis for describing the surface layer of gravel beds. Prog. Phys. Geogr., 43(2), 260-281.

Nield, J.M., King, J. and Jacobs, B. (2014) Detecting surface moisture in aeolian environments using terrestrial laser scanning. Aeolian Res., 12, 9-17.

Owers, C.J., Rogers, K. and Woodroffe, C.D. (2018) Terrestrial laser scanning to quantify above-ground biomass of structurally complex coastal wetland vegetation. Estuar. Coast. Shelf Sci., 204, 164-176.

Park, C.S. and Hwang, E.K. (2011) An investigation of the relationship between sediment particles size and the development of green algal mats (Ulva prolifera) on the intertidal flats of Muan, Korea. J. Appl. Phycol., 23(3), 515-522.

Park, N.W. (2019) Geostatistical integration of field measurements and multi-sensor remote sensing images for spatial prediction of grain size of intertidal surface sediments. J. Coastal Res., 90(SI), 190-196.

Persson, Å., Söderman, U., Töpel, J. and Ahlberg, S. (2005) Visualization and analysis of full-waveform airborne laser scanner data. International Archives of Photogrammetry, Remote Sensing and Spatial Information Sciences, 36(3/W19), 103-108.

Rainey, M.P., Tyler, A.N., Gilvear, D.J., Bryant, R.G. and McDonald, P. (2003) Mapping intertidal estuarine sediment grain size distributions through airborne remote sensing. Remote Sens. Environ., 86(4), 480-490.

Rai, A.K. and Kumar, A. (2019) Determination of the particle load based on detailed suspended sediment measurements at a hydropower plant. Int. J. Sediment Res., 34(5), 409-421.

Rayner, D., Glamore, W., Grandquist, L., Ruprecht, J., Waddington, K. and Khojasteh, D. (2021) Intertidal wetland vegetation dynamics under rising sea levels. Sci. Total Environ., 766, 144237.

Rosser, N.J., Petley, D.N., Lim, M., Dunning, S.A. and Allison, R. J. (2005) Terrestrial laser scanning for monitoring the process of hard rock coastal cliff erosion. Q. J. Eng. Geol.

Hydrogeol., 38(4), 363-375.

Richard Allen, T., Wang, Y. and Gore, B. (2013) Coastal wetland mapping combining multi-date SAR and LiDAR. Geocarto Int., 28(7), 616-631.

Schmid, K.A., Hadley, B.C. and Wijekoon, N. (2011) Vertical accuracy and use of topographic LIDAR data in coastal marshes. J. Coastal Res., 27(6A), 116-132.

Short, A.D. (1991) Macro-meso tidal beach morphodynamics: an overview. J. Coast. Res., 417-436.

Stal, L.J. (2010) Microphytobenthos as a biogeomorphological force in intertidal sediment stabilization. Ecol. Eng., 36(2), 236-245.

Sun, Y.M., Cai, Z.Q. and Fu, J. (2019) Particle morphomics by high-throughput dynamic image analysis. Sci. Rep., 9(1), 1-11.

Swales, A., MacDonald, I.T. and Green, M.O. (2004) Influence of wave and sediment dynamics on cordgrass (Spartina anglica) growth and sediment accumulation on an exposed intertidal flat. Estuaries, 27(2), 225-243.

Swithenbank, J., Beer, J. M., Taylor, D., Abbot, D. and McCreath, G.C. (1976) A laser diagnostic technique for the measurement of droplet and particle size distribution. Progr. of Astronaut. and Aeronaut., 53, 421-447.

Tang, Z.H., Gu, Y., Dai, Z.J., Li, Y., LaGrange, T., Bishop, A. and Drahota, J. (2015) Examining playa wetland inundation conditions for National Wetland Inventory, Soil Survey Geographic database, and LiDAR data. Wetlands, 35(4), 641-654.

Tang, Z.H., Li, R.P., Li, X., Jiang, W.G. and Hirsh, A. (2014) Capturing LiDAR-Derived Hydrologic Spatial Parameters to Evaluate Playa Wetlands. J. Am. Water Resour. Assoc., 50(1), 234-245.

Tseng, K.H., Kuo, C.Y., Lin, T.H., Huang, Z.C., Lin, Y.C., Liao, W.H. and Chen, C.F. (2017) Reconstruction of time-varying tidal flat topography using optical remote sensing imageries. ISPRS-J. Photogramm. Remote Sens., 131, 92-103.

Tulldahl, H.M. and Wikström, S.A. (2012) Classification of aquatic macrovegetation and substrates with airborne lidar. Remote Sens. Environ., 121, 347-357.

Tysmans, D., Claeys, P., Deriemaeker, L., Maes, D., Finsy, R. and Van Molle, M. (2006) Size and shape analysis of sedimentary grains by automated dynamic image analysis. Part. Part. Syst. Charact., 23(5), 381-387.

van de Koppel, J., Herman, P.M., Thoolen, P. and Heip, C. H. (2001). Do alternate stable states occur in natural ecosystems? Evidence from a tidal flat. Ecology, 82(12), 3449-3461.

van Der Wal, D., Herman, P.M. and Wielemaker-van Den Dool, A. (2005) Characterisation of surface roughness and sediment texture of intertidal flats using ERS SAR imagery. Remote Sens. Environ., 98(1), 96-109.

van Leeuwen, B., Augustijn, D.C., Van Wesenbeeck, B.K., Hulscher, S.J. and De Vries, M.B. (2010) Modeling the influence of a young mussel bed on fine sediment dynamics on an intertidal flat in the Wadden Sea. Ecol. Eng., 36(2), 145-153.

van Leeuwen, M., Hilker, T., Coops, N.C., Frazer, G., Wulder, M.A., Newnham, G.J. and Culvenor, D.S. (2011) Assessment of standing wood and fiber quality using ground and airborne laser scanning: a review. For. Ecol. Manage., 261(9), 1467-1478.

Wang, J., Dai, Z.J., Wei, W., Ge, Z.P., Pang, W.H., Ma, B.B., Mei, X.F. and Yu, Y.W. (2018) LiDAR-based recent morphodynamic study of south Nanhui tidal flat, Changjiang Estuary.

Oceanogr. Limnol., 49 (4), 754-768. (in Chinese with English abstract)

Wang, J., Dai, Z.J., Mei, X.F. and Fagherazzi, S. (2020). Tropical cyclones significantly alleviate mega-deltaic erosion induced by high riverine flow. Geophysical Research Letters, 47(19), e2020GL089065.

Wang, X. and Ke, X. (1997) Grain size characteristics of the extant tidal flat sediments along the Jiangsu coast, China. Sediment. Geol., 112(1-2), 105-122.

Ward, R.D., Burnside, N.G., Joyce, C.B. and Sepp, K. (2013) The use of medium point density LiDAR elevation data to determine plant community types in Baltic coastal wetlands. Ecol. Indic., 33, 96-104.

Watson, E. B., Pasternack, G. B., Gray, A. B., Goñi, M. and Woolfolk, A. M. (2013) Particle size characterization of historic sediment deposition from a closed estuarine lagoon, Central California. Estuar. Coast. Shelf Sci., 126, 23-33.

Wei, W., Dai, Z.J, Mei, X.F., Gao, S. and Liu, J.P. (2019). Multi-decadal morpho-sedimentary dynamics of the largest Changjiang estuarine marginal shoal: Causes and implications. Land Degrad. Dev., 30(17), 2048-2063.

Wei, W., Dai, Z.J., Pang, W.H, Wang, J. and Gao, S. (2020) Sedimentary zonation shift of tidal flats in a meso-tidal estuary. Sediment. Geol., 407, 105749.

Wiggins, M., Scott, T., Masselink, G., Russell, P. and McCarroll, R.J. (2019) Coastal embayment rotation: Response to extreme events and climate control, using full embayment surveys. Geomorphology, 327, 385-403.

Wooldridge, L.J., Worden, R.H., Griffiths, J., Utley, J.E. and Thompson, A. (2018). The origin of clay-coated sand grains and sediment heterogeneity in tidal flats. Sediment. Geol., 373, 191-209.

Yamashita, S., Nakajo, T., Naruse, H. and Sato, T. (2009) The three-dimensional distribution of sedimentary facies and characteristics of sediment grain size distribution in a sandy tidal flat along the Kushida River estuary, Ise Bay, central Japan. Sediment. Geol., 215(1-4), 70-82.

Yates, M.G., Jones, A.R., McGrorty, S. and Goss-Custard, J.D. (1993) The use of satellite imagery to determine the distribution of intertidal surface sediments of the Wash, England. Estuar. Coast. Shelf Sci., 36(4), 333-344.

Yoon, J.S., Shin, J.I. and Lee, K.S. (2008) Land cover characteristics of airborne LiDAR intensity data: A case study. IEEE Geosci. Remote Sens. Lett., 5(4), 801-805.

Yoo, J.W., Hwang, I.S. and Hong, J.S. (2007) Inference models for tidal flat elevation and sediment grain size: a preliminary approach on tidal flat microbenthic community. Ocean Sci. J., 42(2), 69-79.

Zhang, C.H., Wang, L.J., Li, G.S., Dong, S.S., Yang, J.R. and Wang, X.L. (2002) Grain size effect on multi-element concentrations in sediments from the intertidal flats of Bohai Bay, China. Appl. Geochem., 17(1), 59-68.

Zhu, Q., Yang, S.L. and Ma, Y.X. (2014) Intra-tidal sedimentary processes associated with combined wave-current action on an exposed, erosional mudflat, southeastern Yangtze River Delta, China. Mar. Geol., 347, 95-106.

Figure captions

Fig. 1. Study area. (a) Location of the Yangtze River in Asia. (b) Three-order bifurcated distributaries of the Yangtze Estuary. The Nanhui tidal flat studied here is located on the southern marginal tidal flat showed in the red rectangle. Artificial reclamation projects (blue dashed curve) and Donghai Bridge near the Nanhui tidal flat are also indicated. (c) Observation station of the Terrestrial Laser Scanner (TLS, Riegl VZ-4000) on the seawall, and the distribution of surface sediment sampling sites. The 20 magenta hollow squares and 5 white dotted lines indicate the transects of the experimental sampling sites, and 5 blue solid squares (m1/v1 to m5/v5) indicate the monthly and validation sampling sites (Table 1). (d) Original intensity of TLS echo, a rectangular area was set to study the relationship between sediment grain size calculated with TLS echo and measured in the laboratory.

Fig. 2. Flow charts for data processing and analysis. Mainly data processing includes three parts: sediment grain size measurements, corrections of waveform amplitude of TLS echoes and multi-parameter function relationship determinations. Finally, discuss the verifications of those constructed relationships and analyze the potential influencing factors.

Fig. 3. Frequency distribution of sediment grain size (0-300 μm) of the 20 experimental samples collected on Jun. 22, 2019, the clay fraction of all sediments was low. (a) site: s01-s06; (b) site: s07-s11; (c) site: s12-s17 and (d) site: s18-s20. (e) Folk's triangle classification of experimental sediments, and (f) nomenclature of sediments collected on Jan. 23, 2019 (winter, green asterisks) and on Jul. 19, 2019 (summer, blue asterisks), respectively.

Fig. 4. (a) Original and corrected waveform amplitudes of TLS echo and corresponding elevation at each experimental sediment sampling site, 5 transects were set in Nanhui tidal flat and shown in Fig. 1c. (b) Original and corrected TLS echo intensity and corrected waveform amplitude of each monthly sediment sampling site.

Fig. 5. Relationships between the corrected waveform amplitudes of TLS echo and three sediment fractions, (a) sand fraction, (b) silt fraction and (c) clay fraction. The logarithmic fitting curves were calculated based on all sediment data that collected in the experimental and monthly sites, and the 95% confidence intervals are also indicated.

Fig. 6. Fig. 6. Relationships between the corrected waveform amplitudes of TLS echo and the (a) sediment average grain size and (b) sediment D50. The different logarithmic fitting curves and related confidence intervals for experiment and monthly sediments, respectively, are shown in (c) for sediment average grain size and (d) for sediment D50.

Fig. 7. Comparison of indoor measured and TLS-based calculated sediment parameters (sand fraction, silt fraction, average grain size and D50), calculated results were based on constructed log-fitting equations between the corrected waveform amplitudes of TLS echo and the sediment parameters. (a-d) All experimental and monthly sediment samples; (e-f) at five monthly sampling sites, standard deviations were also indicated.

Fig. 8. A logarithm fitting equation $y=a*ln(x)+b$ was used to determine relationship the between corrected waveform amplitude and the sediment average grain size, specific results were shown in Table S1. (a-b) Relationship between correlation coefficient (r) and parameters a and b of the logarithm fitting equation. (c-e) Relationship between intertidal slope and correlation coefficient (r), parameter a and parameter b, respectively.

Fig. 9. (a-d) Logarithmic fittings of validations between the corrected waveform amplitudes of TLS echo and different sediment fraction and grain sizes, the data were collected independently of experimental and monthly samples, and then compared with the study results. (e-f) Comparison of measured and TLS-based calculated sediment parameters (sand fraction, silt fraction, average grain size and D_{50}), calculated results were based on the above constructed log-fitting equations of study results.

Fig. 10. (a-b) The spatial distribution of sediment average grain size in June 2019, that were derived from indoor measured and TLS-based calculated result, respectively, then a total of 550 equally spaced points are generated to analyze the difference between the two. (c) The relationship between measured and TLS-based calculated average grain sizes. (d) TLS-based calculated average grain sizes in January 2019 and (e) frequency distribution of TLS-based results in January and June 2019.

Table captions

Table 1. Dates of sediment sampling and TLS observation of different data sets.

Table 2. Multi-grain size parameters of intertidal surface sediment of the experimental set.

Table 3. Measured water content of intertidal surface sediments of the experimental set.

Table 4. Comparison of indoor measured and TLS-based calculated three fractions (sand, silt and clay), average grain size and D_{50} of surface sediment at different monthly sampling sites.

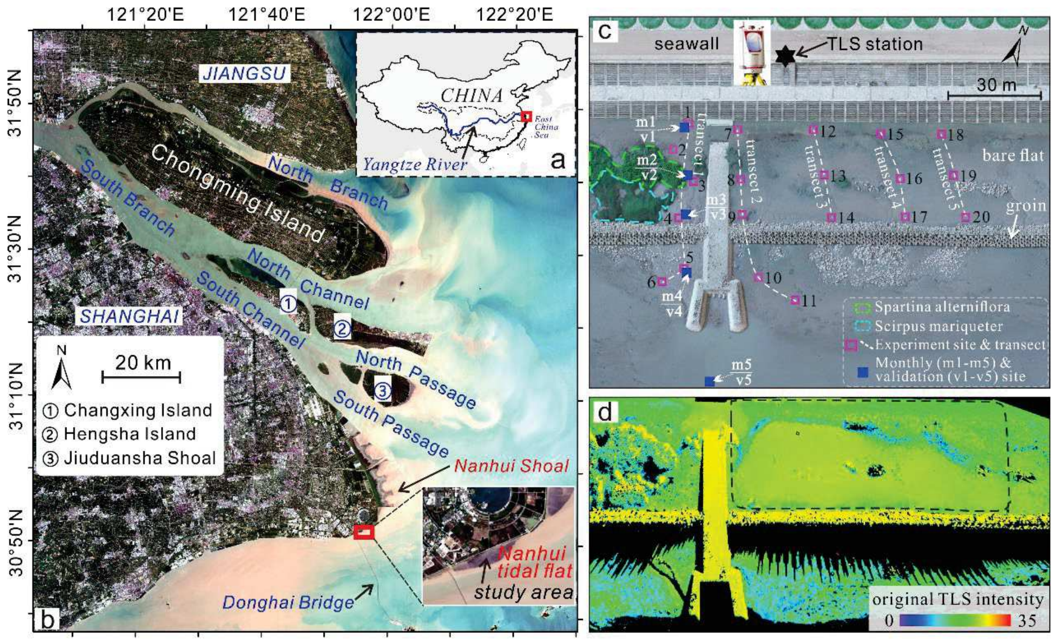

Fig. 1. Study area. (a) Location of the Yangtze River in Asia. (b) Three-order bifurcated distributaries of the Yangtze Estuary. The Nanhui tidal flat studied here is located on the southern marginal tidal flat showed in the red rectangle. Artificial reclamation projects (blue dashed curve) and Donghai Bridge near the Nanhui tidal flat are also indicated. (c) Observation station of the Terrestrial Laser Scanner (TLS, Riegl VZ-4000) on the seawall, and the distribution of surface sediment sampling sites. The 20 magenta hollow squares and 5 white dotted lines indicate the transects of the experimental sampling sites, and 5 blue solid squares (m1/v1 to m5/v5) indicate the monthly and validation sampling sites (Table 1). (d) Original intensity of TLS echo, a rectangular area was set to study the relationship between sediment grain size calculated with TLS echo and measured in the laboratory.

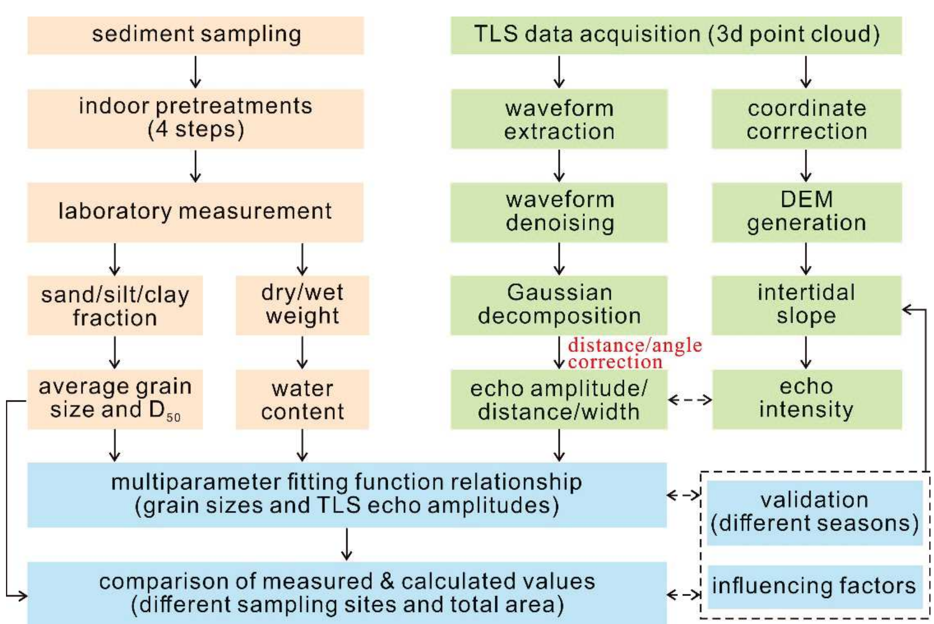

Fig. 2. Flow charts for data processing and analysis. Mainly data processing includes three parts: sediment grain size measurements, corrections of waveform amplitude of TLS echoes and multi-parameter function relationship determinations. Finally, discuss the verifications of those constructed relationships and analyze the potential influencing factors.

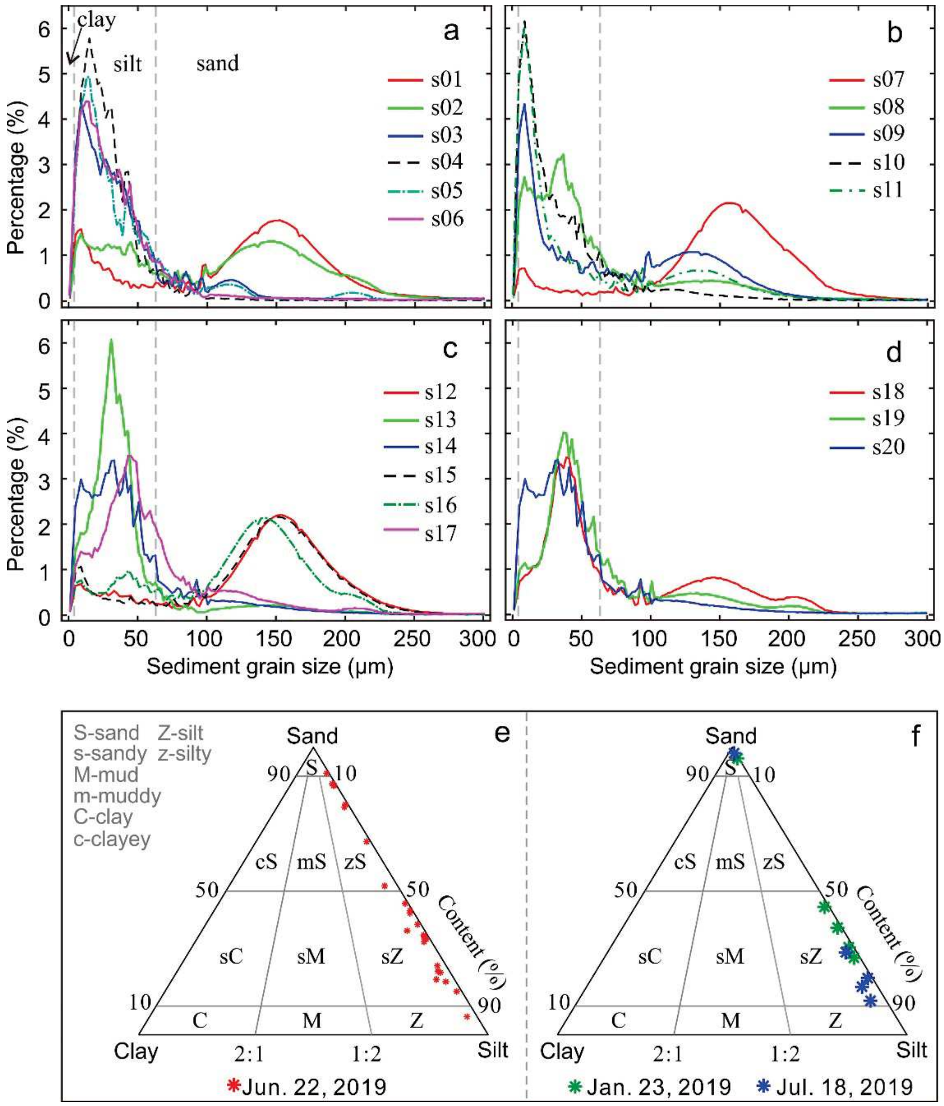

Fig. 3. Frequency distribution of sediment grain size (0-300 μm) of the 20 experimental samples collected on Jun. 22, 2019, the clay fraction of all sediments was low. (a) site: s01-s06; (b) site: s07-s11; (c) site: s12-s17 and (d) site: s18-s20. (e) Folk's triangle classification of experimental sediments, and (f) nomenclature of sediments collected on Jan. 23, 2019 (winter, green asterisks) and on Jul. 19, 2019 (summer, blue asterisks), respectively.

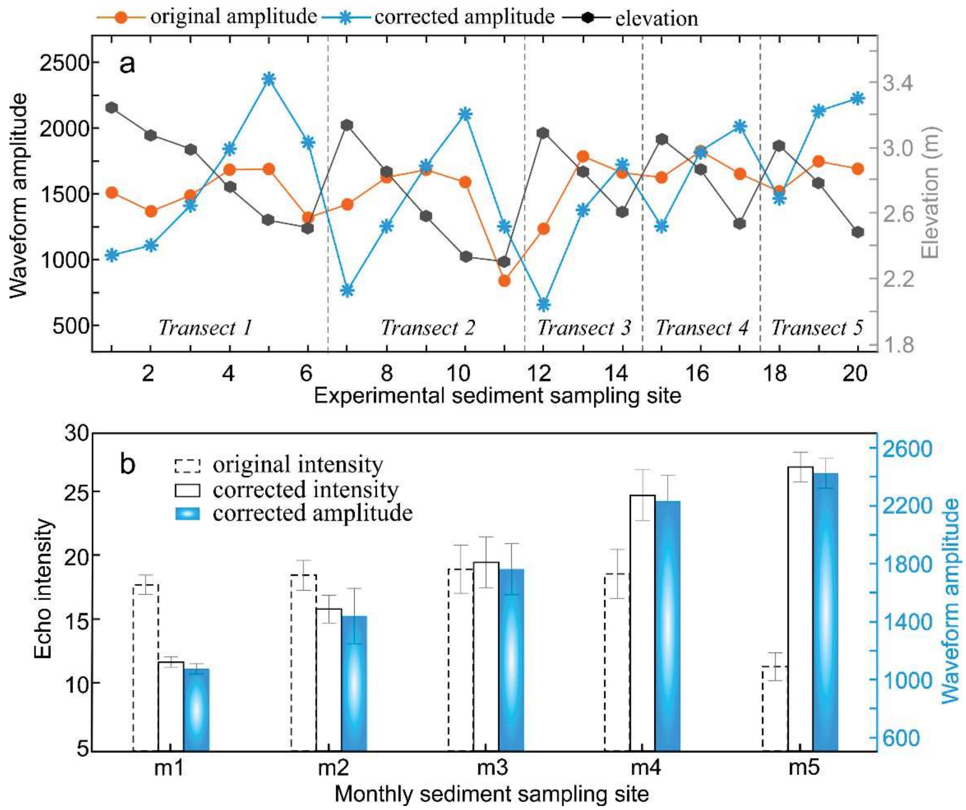

Fig. 4. (a) Original and corrected waveform amplitudes of TLS echo and corresponding elevation at each experimental sediment sampling site, 5 transects were set in Nanhui tidal flat and shown in Fig. 1c. (b) Original and corrected TLS echo intensity and corrected waveform amplitude of each monthly sediment sampling site.

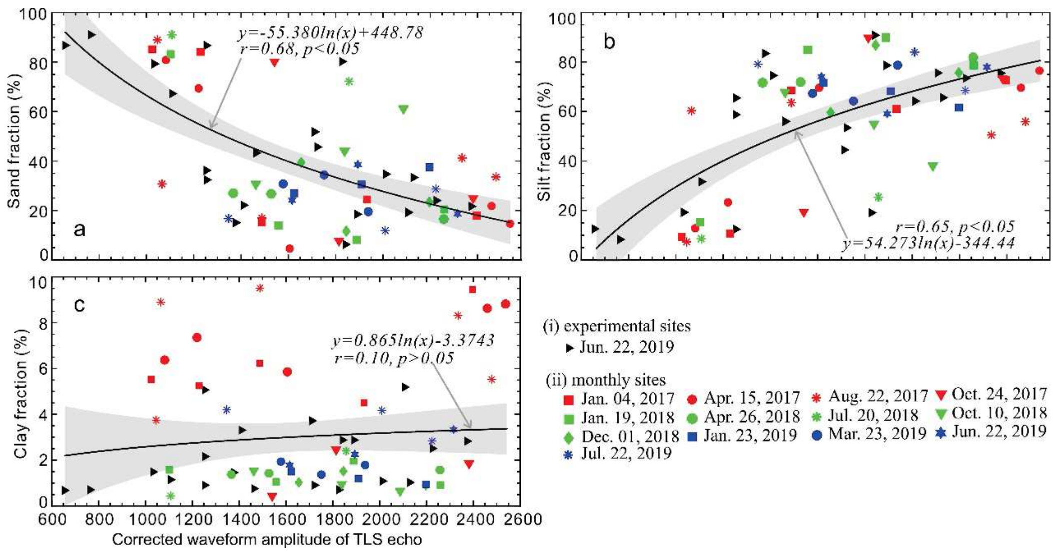

Fig. 5. Relationships between the corrected waveform amplitudes of TLS echo and three sediment fractions, (a) sand fraction, (b) silt fraction and (c) clay fraction. The logarithmic fitting curves were calculated based on all sediment data that collected in the experimental and monthly sites, and the 95% confidence intervals are also indicated.

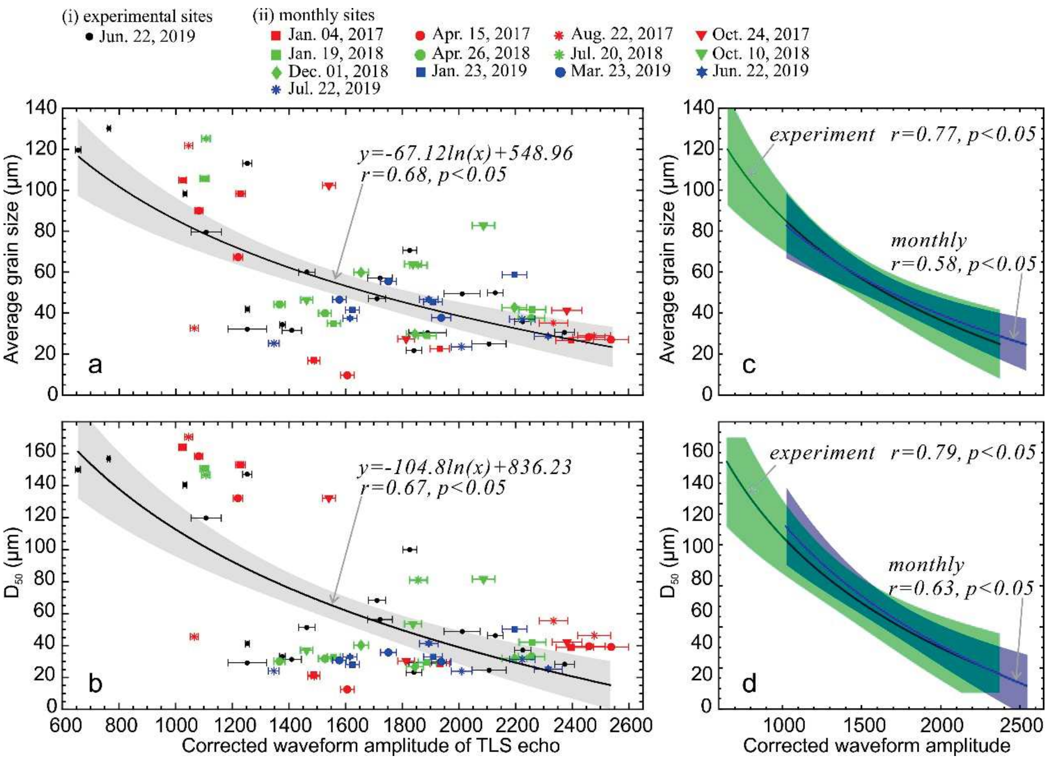

Fig. 6. Relationships between the corrected waveform amplitudes of TLS echo and the (a) sediment average grain size and (b) sediment D_{50}. The different logarithmic fitting curves and related confidence intervals for experiment and monthly sediments, respectively, are shown in (c) for sediment average grain size and (d) for sediment D_{50}.

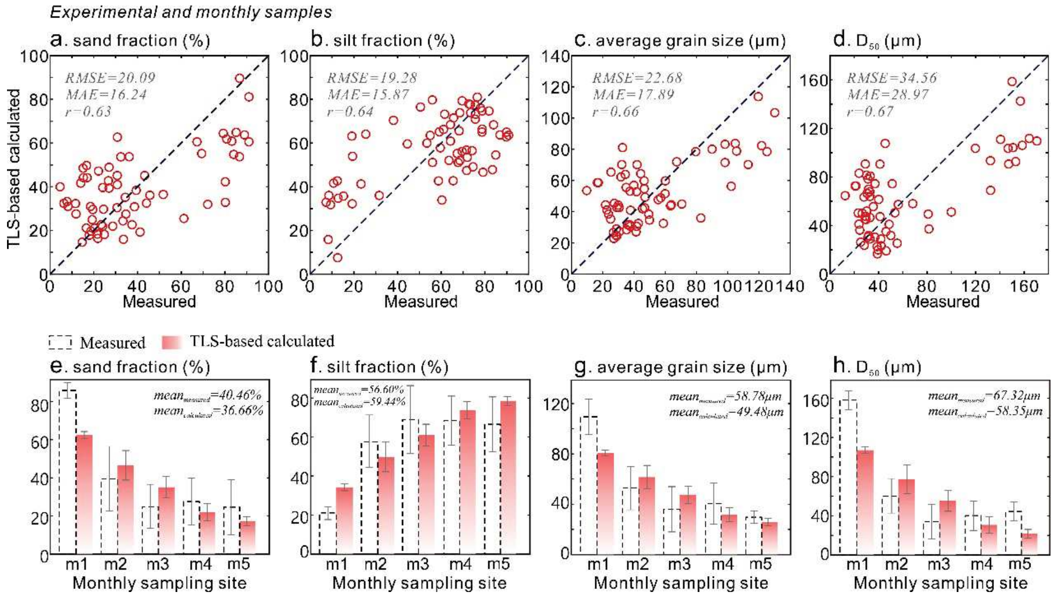

Fig. 7. Comparison of indoor measured and TLS-based calculated sediment parameters (sand fraction, silt fraction, average grain size and D_{50}), calculated results were based on constructed log-fitting equations between the corrected waveform amplitudes of TLS echo and the sediment parameters. (a-d) All experimental and monthly sediment samples; (e-f) at five monthly sampling sites, standard deviations were also indicated.

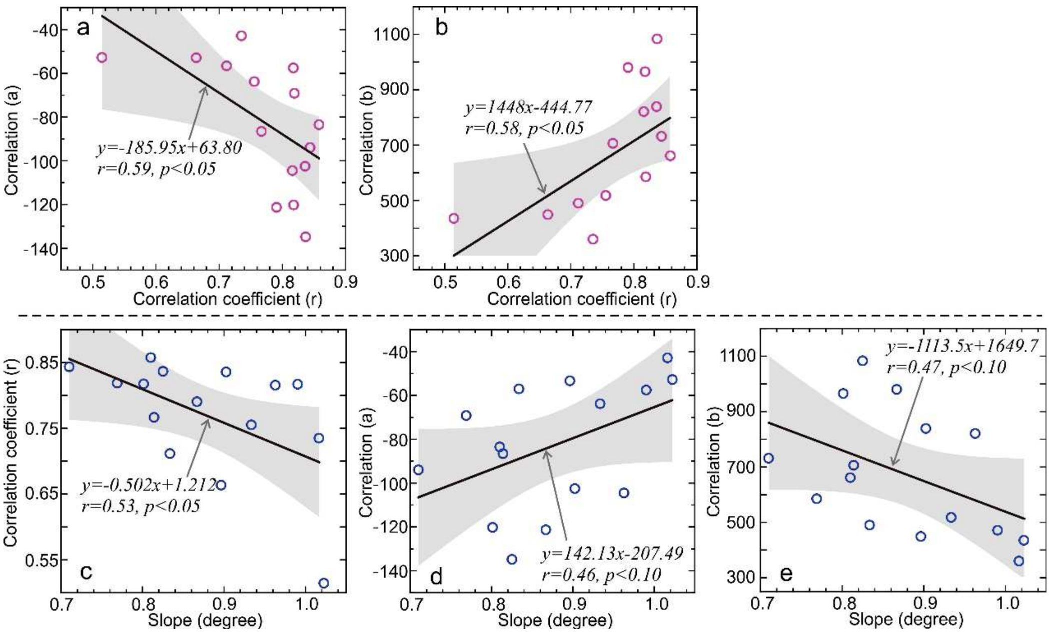

Fig. 8. A logarithm fitting equation $y=a*ln(x)+b$ was used to determine relationship the between corrected waveform amplitude and the sediment average grain size, specific results were shown in Table S1. (a-b) Relationship between correlation coefficient (*r*) and parameters *a* and *b* of the logarithm fitting equation. (c-e) Relationship between intertidal slope and correlation coefficient (*r*), parameter *a* and parameter *b*, respectively.

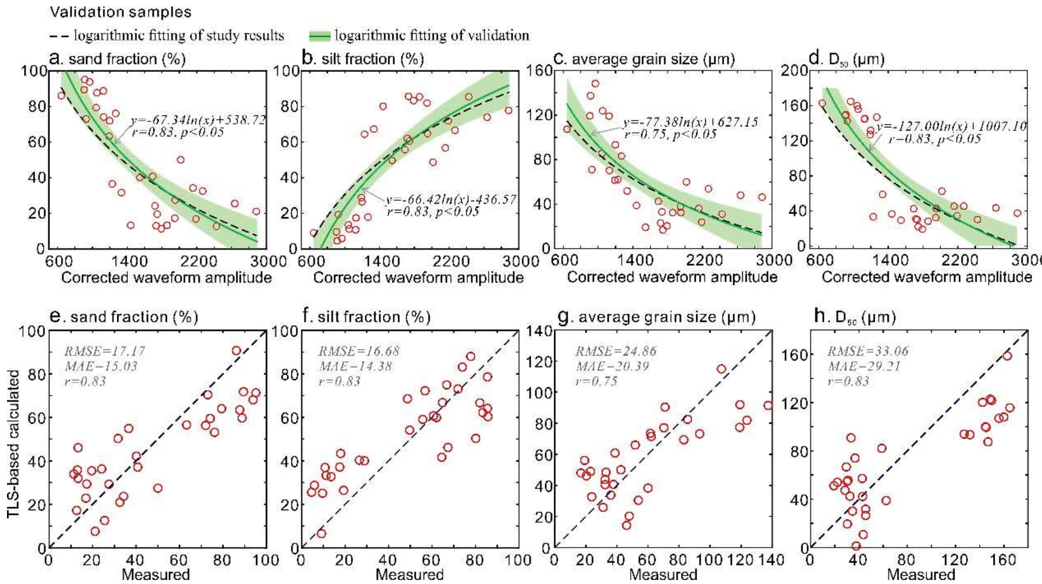

Fig. 9. (a-d) Logarithmic fittings of validations between the corrected waveform amplitudes of TLS echo and different sediment fraction and grain sizes, the data were collected independently of experimental and monthly samples, and then compared with the study results. (e-f) Comparison of measured and TLS-based calculated sediment parameters (sand fraction, silt fraction, average grain size and D50), calculated results were based on the above constructed log-fitting equations of study results.

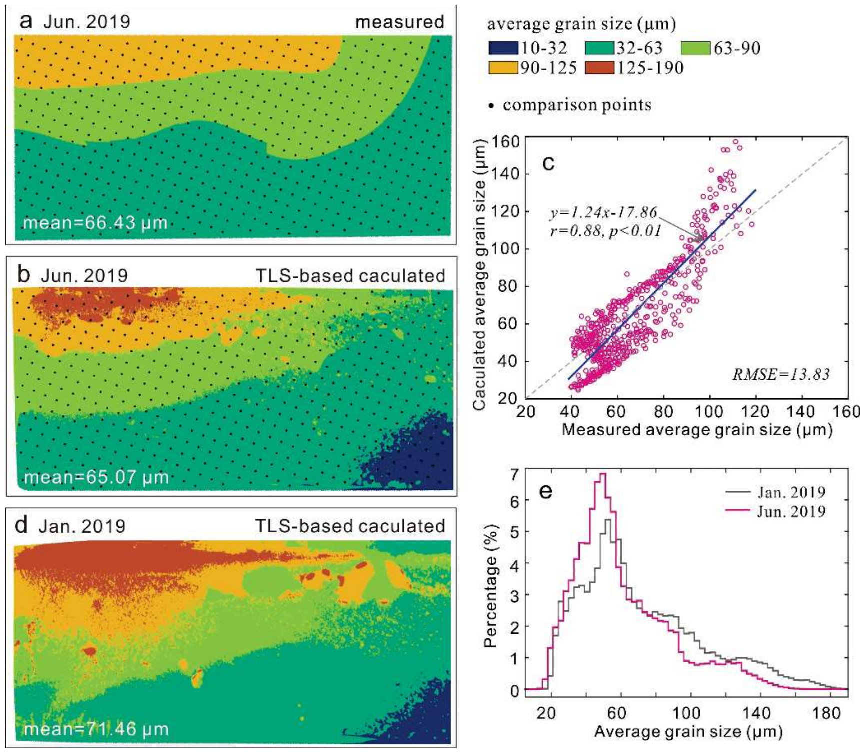

Fig. 10. (a-b) The spatial distribution of sediment average grain size in June 2019, that were derived from indoor measured and TLS-based calculated result, respectively, then a total of 550 equally spaced points are generated to analyze the difference between the two. (c) The relationship between measured and TLS-based calculated average grain sizes. (d) TLS-based calculated average grain sizes in January 2019 and (e) frequency distribution of TLS-based results in January and June 2019.

Table 1. Dates of sediment sampling and TLS observation of different data sets.

Data set		Date
Experiment		Jun. 22, 2019
Monthly		Jan. 04, 2017; Apr. 14, 2017; Aug. 22, 2017; Oct. 24, 2017 Jan. 19, 2018; Apr. 26, 2018; Jul. 20, 2018; Oct. 10, 2018; Dec. 01, 2018 Jan. 23, 2019; Mar. 23, 2019; Jun. 23, 2019; Jul. 22, 2019
Validation	Winter	Dec. 02, 2016; Feb. 13, 2017; Feb. 5, 2018; Feb. 23, 2019
	Summer	May. 13, 2017; Jun. 29, 2018; Aug. 20, 2018; Jul. 18, 2019

Table 2. Multi-grain size parameters of intertidal surface sediment of the experimental set.

Site	Sand fraction (%)	Silt fraction (%)	Clay fraction (%)	Average grain size (μm)	D_{50} (μm)	δ	*Sk*	*Ku*
s01	79.26	19.25	1.49	98.28	140.56	1.55	1.77	2.34
s02	67.22	31.63	1.15	79.52	119.81	1.48	1.57	2.15
s03	22.14	74.55	3.31	31.61	31.32	1.69	0.58	2.33
s04	6.30	90.82	2.88	21.73	23.24	1.17	0.65	1.74
s05	21.68	75.49	2.83	30.62	28.29	1.67	0.62	2.29
s06	18.48	78.64	2.88	30.45	29.46	1.67	0.69	2.38
s07	91.01	8.28	0.71	130.16	156.89	1.10	1.59	2.12
s08	32.38	65.46	2.16	41.92	41.22	1.56	0.83	2.13
s09	51.79	44.49	3.72	47.07	68.22	1.89	1.49	2.39
s10	19.25	75.56	5.19	24.99	24.57	1.73	0.55	2.33
s11	36.20	58.73	5.07	32.16	29.16	1.95	0.63	2.38
s12	86.75	12.57	0.68	119.58	150.02	1.16	1.56	2.09
s13	15.10	83.45	1.46	34.38	33.13	1.27	0.46	1.98
s14	45.67	53.43	0.91	57.13	56.28	1.35	1.11	1.93
s15	86.68	12.41	0.91	113.10	147.23	1.24	1.68	2.21
s16	80.19	19.10	0.71	70.61	100.00	1.17	1.48	1.99
s17	34.70	64.21	1.09	49.43	48.80	1.29	0.82	1.93
s18	43.25	55.99	0.76	1.34	0.92	1.90	60.07	51.31
s19	33.35	65.62	1.03	1.25	0.90	1.88	49.92	46.23
s20	24.03	73.46	2.51	1.51	0.42	2.13	35.85	37.10

Note: δ is sorting factor; *Sk* is skewness and *Ku* is kurtosis of intertidal sediment.

Table 3. Measured water content of intertidal surface sediments of the experimental set.

Site	s01	s02	s03	s04	s05	s06	s07	s08	s09	s10
SWC (%)	20.05	20.66	23.28	28.98	32.03	33.40	18.90	27.27	30.30	32.91
Site	s11	s12	s13	s14	s15	s16	s17	s18	s19	s20
SWC (%)	34.51	20.93	23.68	22.97	23.91	17.89	22.34	27.13	25.98	26.16

Note: *SWC* is the sediment water content.

Table 4. Comparison of indoor measured and TLS-based calculated three fractions (sand, silt and clay), average grain size and D_{50} of surface sediment at different monthly sampling sites.

	Site	m1	m2	m3	m4	m5	Mean of all absolute errors	Mean of all sampling sites
Sand fraction	Measured (%)	85.81	39.50	24.83	27.56	24.61	/	40.46
	Calculated (%)	62.38	46.56	35.09	22.04	17.25	/	36.66
	Error (%)	-27.30	17.87	41.32	-20.03	-29.91	27.28	-9.39
Silt fraction	Measured (%)	21.66	57.47	68.92	68.41	66.53	/	56.6
	Calculated (%)	34.23	49.74	60.98	73.77	78.46	/	59.44
	Error (%)	58.03	-13.45	-11.52	7.84	17.93	21.75	5.01
Clay fraction	Measured (%)	3.53	3.03	3.18	2.79	8.86	/	4.28
	Calculated (%)	2.66	2.91	3.09	3.29	5.87	/	3.56
	Error (%)	-24.65	-3.96	-2.83	17.92	-33.75	16.62	-16.69
Average grain size	Measured (μm)	109.48	53.08	35.99	40.69	29.67	/	58.78
	Calculated (μm)	80.65	61.48	47.58	31.76	25.95	/	49.48
	Error (%)	-26.33	15.83	32.20	-21.95	-12.54	21.77	-7.99
D_{50}	Measured (μm)	158.13	59.92	33.93	40.17	44.45	/	67.32
	Calculated (μm)	107.02	77.08	55.38	30.68	21.61	/	58.35
	Error (%)	-32.32	28.64	63.22	-23.62	-51.38	39.83	-13.32